

Andrey A. Gurenko · Alexander V. Sobolev

Crust–primitive magma interaction beneath neovolcanic rift zone of Iceland recorded in gabbro xenoliths from Midfell, SW Iceland

Received: 31 August 2005 / Accepted: 15 February 2006 / Published online: 25 March 2006
© Springer-Verlag 2006

Abstract We studied glass-bearing gabbro xenoliths from picritic pillow lavas erupted in the Midfell area, SW Iceland. The aim of this study is to investigate the processes affecting chemical composition of primitive Icelandic magmas at crustal depths. The xenoliths formed at 340 ± 160 MPa (2σ) lithostatic pressure are cumulates of earlier crystallized magmas. Later interaction of the xenoliths with the transporting magmas occurred at $1,190$ – $1,230^\circ\text{C}$ and shallower depths (40 ± 120 MPa). The xenoliths consist of reversely zoned, slightly resorbed, subhedral plagioclase (PL, An_{81-90} , 50–60%), anhedral, strongly resorbed clinopyroxene (CPX, mg -number = 83–90, 25–32%), trace amounts (<1%) of small, up to 500 μm , euhedral olivine (OL, Fo_{85-89}) and spinel (SP, mg -number = 66–73, cr -number = 29–51), and interstitial glass (9–22%). No significant difference in chemical composition between surrounding host pillow rim glasses ($\text{K}_2\text{O}/\text{TiO}_2 = 0.02$ – 0.04 , $\text{CaO}/\text{Al}_2\text{O}_3 = 0.93$ – 1.04 , $[\text{La}/\text{Sm}]_n = 0.38$ – 0.54 , where subscript n points on element concentrations normalized to those in chondrite) and interstitial glasses ($\text{K}_2\text{O}/\text{TiO}_2 = 0.03$ – 0.06 , $\text{CaO}/\text{Al}_2\text{O}_3 = 1.00$ – 1.07 , $[\text{La}/\text{Sm}]_n = 0.41$ – 0.74) was recognized. Deep glassy embayments in CPX ($\text{K}_2\text{O}/\text{TiO}_2 = 0.02$ – 0.06 , $\text{CaO}/\text{Al}_2\text{O}_3 = 1.00$ – 1.06 , $[\text{La}/\text{Sm}]_n = 0.66$ – 0.99) have also chemical compositions very close to those of interstitial and host glasses. Glass embayments in PL ($\text{K}_2\text{O}/\text{TiO}_2 = 0.03$ – 0.11 , $\text{CaO}/\text{Al}_2\text{O}_3 = 0.87$ – 1.06 , $[\text{La}/\text{Sm}]_n = 0.70$ – 0.97) vary more significantly in $\text{CaO}/\text{Al}_2\text{O}_3$ ratios than those in CPX likely due to their

stronger modification by post-entrapment crystallization. All glass types, regardless of whether they are enclosed in minerals or represent interstitial or host matrix glasses, are characterized by significant excess of Sr ($[\text{Sr}/\text{Sr}^*]_n = 1.7$ – 2.7) but not of Ba relative to Nb ($[\text{Ba}/\text{Nb}]_n = 0.45$ – 0.96). Partial melting of a gabbro with $[\text{La}/\text{Sm}]_n = 0.54$, $[\text{Sr}/\text{Sr}^*]_n = 10.5$ and $[\text{Ba}/\text{Nb}]_n = 4.5$ inferred from the composition of the xenoliths studied cannot account for the observed trace element concentrations and ratios in the associated glasses. In fact, the compositions of melts calculated for 1–40% of partial melting match neither compositions of the interstitial glasses nor CPX- and PL-hosted glassy embayments with respect to $[\text{Ba}/\text{Nb}]_n$ ratios. Mixing of these partial melts with presumably uncontaminated magma composition does not explain chemical variations observed in the glasses as well. In contrast, the model of melt percolation through gabbroic matrix reproduces in a satisfactory way the compositions of glasses. We believe that the pronounced enrichment in Sr relative to other trace elements of similar incompatibility observed in many Icelandic tholeiites and probably in many MORB-type magmas worldwide could result from such interaction of the ascending magmas with gabbroic cumulates at crustal depths. We emphasize that the percolation model discussed here results in hybrid, Sr-enriched magmas which are saturated with CPX and PL. The enrichment in Sr of PL-undersaturated melts (so-called “ghost plagioclase signature”; Sobolev et al. in Nature 404:986–990, 2000) could not be produced by such percolation process.

Communicated by J. Hoefs

A. A. Gurenko (✉) · A. V. Sobolev
Max-Planck-Institut für Chemie, Abteilung Geochemie,
Postfach 3060, 55020 Mainz, Germany
E-mail: agurenko@mpch-mainz.mpg.de
Tel.: +49-6131-305304
Fax: +49-6131-371051

A. V. Sobolev
Vernadsky Institute of Geochemistry and Analytical Chemistry,
Russian Academy of Sciences, Kosygin Str 19, 119991 Moscow,
Russia

Keywords Iceland · Gabbro xenoliths · Petrology · Geochemistry · Major and trace elements · Melt percolation

Introduction

Primitive magmas may only adequately reflect the composition of their mantle source and conditions of

origin, if they remain preserved from later interaction with surrounding rocks at shallower depths. However, such interactions appear to be very common when magmas pass through thick lithosphere or crystal mush residing in the magma chamber (e.g., Marsh 1995, 1998). Iceland represents a plume centered on the mid-ocean ridge and is characterized by anomalously thick oceanic crust (e.g., Darbyshire et al. 2000 and references therein). Gabbroic rocks and greenschist metamorphosed amphibolites are main constituents of Layer 3 in the Icelandic crust (Pálmason 1971; Christensen 1974; Oskarsson et al. 1985; Steinthorsson et al. 1985; Flóvenz and Gunnarsson 1991), while mixture of primitive olivine–normative tholeiitic magmas with silica-rich partial melts produced during anatexis of crustal amphibolites is suggested as a possible mechanism for the origin of Icelandic alkali basaltic magmas (e.g., Oskarsson et al. 1982, 1985; Steinthorsson et al. 1985). Hence, interaction of the ascending magmas with crustal rocks or contamination of primitive, mantle-derived magmas could be more common in Iceland compared to mid-ocean ridge basalts (MORB). This makes Iceland ideally suited for the studies of processes of melt–rock interaction at crustal depths.

Many Icelandic tholeiitic lavas are characterized by significant Sr excess relative to other trace elements of similar incompatibility such as Ce and Nd (e.g., Hémond et al. 1993; Gurenko and Chaussidon 1995 and references therein). These rocks commonly have higher CaO and lower Al₂O₃ contents compared to primitive mid-ocean ridge basalts (e.g., Jakobsson et al. 1978; Risku-Norja 1985; Gurenko et al. 1988, 1990; Trønnes 1990). Several processes are proposed to explain the observed geochemical signatures: (1) contamination of melts by plagioclase-rich material either through bulk assimilation or wall rock melting (see discussion in Hémond et al. 1993), (2) mobilization of Rb, Sr and Ba from secondary carbonate veins at crustal depths in the close vicinity to magma reservoir (Hémond et al. 1993), (3) interaction of the ascending magmas with crystal matrix in the plagioclase-rich cumulates occurred in the magma chamber (Sobolev et al. 1992, 1994; Gurenko and Chaussidon 1995), (4) partial melting of plagioclase-bearing peridotite mantle (Gurenko and Chaussidon 1995), and (5) presence of the recycled crustal component in the Icelandic plume (Chauvel and Hémond 2000; Skovgaard et al. 2001; Gurenko and Chaussidon 2002). All earlier listed processes have significant constraints on major and trace element compositions of the resulted melts that sometimes are difficult to assess quantitatively. In particular, the origin of Sr anomaly due to melting of plagioclase-bearing mantle source, as suggested by Gurenko and Chaussidon (1995), anticipates presence of plagioclase as a residual phase up to high melting degrees, whereas plagioclase appears to be exhausted from the source at less than 4% of partial melting, as it follows from the experimental data by Falloon et al. (1999).

Our work addresses the problems of melt–rock interaction occurred in the Icelandic crust. We present petrologic and geochemical data from glass-bearing gabbro nodules that are abundant in the picritic pillow lavas erupted from the Midfell volcano, SW Iceland. It is essential that Midfell lavas are characterized by the largest Sr enrichment in the chondrite-normalized trace element spectra among other Icelandic tholeiites. Gabbroic nodules in Icelandic lavas were studied previously by several authors (Thórarinnsson 1953; Tryggvason 1960; Jakobsson 1966, 1979; Jakobsson et al. 1973; Kristmannsdóttir 1971; Larsen 1979; Pedersen and Hald 1982; Höj 1993; Risku-Norja 1985; Sigurdsson 1989; Hansteen 1991; Genshaft and Saltykovsky 1999). One group of nodules (i.e., the gabbro nodules from Krisuvik) was interpreted as true crustal xenoliths (Thórarinnsson 1953; Tryggvason 1960; Höj 1993), while the other group was considered to be cognate to the confining magma (Larsen 1979; Risku-Norja 1985; Sigurdsson 1989; Hansteen 1991). In relatively rare cases, gabbroic nodules found in picritic lavas display signatures of extended partial melting and mineral resorption (Larsen 1979; Risku-Norja 1985; Hansteen 1991). In this context, the Midfell area, SW Iceland (Fig. 1) represents a key locality for understanding the origin of Sr excess in basaltic magmas because (1) there are abundant fragments of partially to completely disintegrated gabbroic cumulates and individual gabbro xenoliths in picritic pillow lavas, (2) the most pronounced Sr excess in chondrite-normalized trace element spectra is a signature of the Midfell rocks and glasses among a large number of Icelandic tholeiites in general (the latter is outlined in Fig. 7), and (3) the presence of very well quenched glass inside and outside gabbro nodules allows in situ analyses of major and trace elements in the melt using microanalytical techniques.

The aim of this study is to focus on the interaction of the ascending magmas with gabbroic crustal rocks. We evaluate quantitatively three concurrent processes i.e., (1) gabbro partial melting, (2) mixing of melts produced by gabbro anatexis with presumably uncontaminated primitive olivine–normative tholeiitic magma and (3) melt percolation through gabbroic rocks. We discuss chromatographic effects on the composition of primitive tholeiitic melts percolating through a crystal mush column located within the Icelandic crust. The results of this work can be used to understand the origin of Icelandic primitive magmas, as well as to revise our understanding of partial melting processes occurred in the Icelandic mantle.

Geological setting

Midfell is a table mountain ca. 320 m high which resulted from sub-glacial fissure eruptions and situated on the eastern shore of the Thingvallavatn Lake (Fig. 1). It

extends about 3 km in SW–NE direction, belongs to the Hengill fissure swarm and consists of two subunits of slightly different age (Risku-Norja 1985). The Midfell itself represents a northeastern, younger part composed mostly of plagioclase-phyric hyaloclastites with rare olivine phenocrysts, while the southwestern part called Dagmálfell is older and composed of picritic pillow lavas located in the upper part of the volcanic sequence. Many of these olivine-, clinopyroxene- and plagioclase-phyric pillow lavas, and hyaloclastites of the Dagmálfell unit contain also large disintegrated plagioclase crystals (10–25 mm), poikilitic pyroxene and plagioclase clusters (up to a few cm in size), as well as rounded gabbroic nodules (up to 10×15 cm) defined as cumulates formed due to magma fractionation (Risku-Norja 1985). Though all xenoliths studied were collected within the Dagmálfell subunit, we use the terms “Midfell gabbro xenoliths” or “Midfell gabbro nodules” throughout the entire text following the classification by Risku-Norja (1985).

The Midfell gabbro xenoliths were subdivided on several main types based on mineral assemblage and volume proportions of the composing minerals. They include (1) plagioclase (PL)–clinopyroxene (CPX)–olivine (OL), (2) plagioclase–clinopyroxene and (3) pure plagioclase-bearing types with averaged modal proportions of 53% PL, 11% CPX, 7% OL and 29% interstitial groundmass (Risku-Norja 1985). No essential difference in chemical composition of nodule-forming minerals and host-rock phenocrysts were observed (Risku-Norja 1985). The origin of Midfell xenoliths was placed to approximately crust-mantle boundary or even to the upper part of the upper mantle; further substantial reaction of these xenoliths with replenishing primitive magma batches was suggested (Risku-Norja 1985).

Methods

Electron microprobe

Major elements in minerals and glasses and element mapping were performed at the Max Planck Institute for Chemistry (Mainz, Germany; hereafter referred as MPI-Mainz) using the JEOL Superprobe JXA-8200 electron microprobe. We applied 15 kV accelerating voltage, 12 nA electron beam current and 1–2 μm size of the beam for analyses of clinopyroxene and plagioclase but defocused to 5 μm during analyses of glasses. The 20 kV and 20 nA primary beam was applied for analyses of olivine and spinel. Either PRZ or ZAF correction routines were used. Peak counting times on major elements were 60 and 30 s of background. Sulfur was analyzed at the same analytical conditions as other major elements in glasses. At these conditions, the detection level for S was around 200–250 ppm. A set of reference materials i.e., natural and synthetic oxides, minerals and glasses (Micro-Analysis Consultants Ltd, Cambridgeshire, UK)

and the Smithsonian Institution standard set for electron microprobe analysis (Jarosewich et al. 1980) were used for routine calibration and instrument stability monitoring. Typical analytical uncertainties ($2\text{RSD} = 2\sigma$ relative standard deviation) are 0.6–1.2% for SiO_2 , Al_2O_3 , FeO , MgO , CaO ; 2–4% for TiO_2 , Na_2O ; 8–10% for K_2O , MnO and 10–20% for P_2O_5 and S. As a monitor sample to control precision and accuracy of S measurements, we used the USNM 111240/52 VG2 basaltic glass (0.134–0.137 wt% S; Dixon et al. 1991; Thordarson et al. 1996); 0.137 ± 0.020 wt% S ($\pm 2\sigma$, $N=109$) was obtained during this study.

Element mapping was performed to examine two-dimensional distribution of elements across sample surface. Measurements were done in the stage scanning mode registering simultaneously X-ray signals of five wavelength dispersive spectrometers and back-scattered electron (BSE) image. We analyzed clinopyroxene for Mg, Al, Ca, Fe and Ti, and plagioclase for Na, Al, Ca, Fe and Si using TAP spectrometers for Si, Mg, Al and Na, PETJ for Ca, LIF for Fe and PETH for Ti, applying 15 kV accelerating voltage and 12 nA primary electron beam current. Step interval was 2 μm and X-ray acquisition time per step was 200–300 ms depending on the square of the map. At such conditions, the duration of a single map analysis varied between 20 and 100 h. Final evaluation of the measurement results were performed using the built-in JEOL Map Analysis Software.

Ion microprobe

Trace elements were analyzed at MPI-Mainz using a CAMECA IMS3f ion microprobe. The conditions were 12.5 kV accelerating voltage of O^- primary beam, 4.5 kV secondary ion accelerating voltage, –80 V offset and mass resolving power $M/\Delta M = 300$. The energy slit was centered and opened to 25 V. A 150 μm contrast aperture and a 1,800 μm field aperture were used. Each

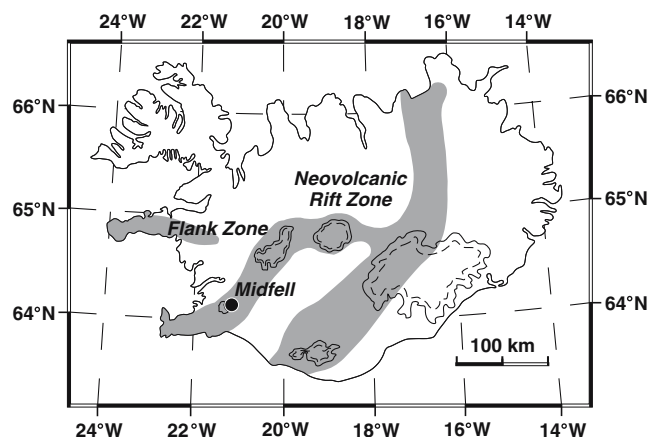


Fig. 1 Schematic map of Iceland showing the active neovolcanic rift and off-rift (*flank*) zones (modified after Jakobsson 1979) and location of sample selection (*filled circle*)

analysis consisted of five scans, starting from ^{16}O mass (using for magnet adjustment), then over the sequence of ^{30}Si , ^{39}K , ^{44}Ca , ^{47}Ti , ^{51}V , ^{52}Cr , ^{88}Sr , ^{89}Y , ^{90}Zr , ^{93}Nb , and then each mass from 133 to 180. The remaining oxide interferences, for example, light rare earth element (LREE) oxides interfering with heavy rare earth elements (HREE), were corrected using peak deconvolution routine based on the approach described by Zinner and Crozaz (1986) and Fahey et al. (1987). Relative sensitivity factors [RSF, defined as the ratio of total ionic intensity for a given element to the ionic intensity of Si divided by the respective element ratios in atomic concentrations; i.e., $(\text{K}^+/\text{Si}^+)/(\text{K}/\text{Si})$] were determined from the analyses of basaltic reference glasses (Jochum et al. 2000). Instrument drift was controlled and correction applied using daily replicate analyses of KL2-G reference glass (Jochum et al. 2000; Table 1). The obtained analytical error was better than 20% (2σ RSE) for all elements except Gd whose uncertainty ranges between 18 and 25% (Table 1).

Major and trace elements in whole rocks

Major and trace elements in whole-rock samples were analyzed using ICP-AES and ICP-MS by Analytical Service of Rocks and Minerals (SARM) at the CRPG-CNRS (Nancy, France; for more technique details, see Carignan et al. 2001). The uncertainties and detection

levels for different elements provided by SARM are given in Table 1. The uncertainty is better than 1–5% for major elements, if their concentrations exceed 1 wt% and 2–10% for element concentrations below 1 wt%. For trace elements, the uncertainty is 5–10% for the concentration range from ca. 0.1 to 1,000 ppm.

Petrography and mineral compositions

We restricted our studies only to those gabbro nodules that contain well-preserved glassy crusts on the surface suggesting their rapid cooling and quenching. The nodules are medium- to coarse-grained holocrystalline to hypocrySTALLINE rocks with hypidiomorphic inequigranular texture (Fig. 2). The gabbro nodules are composed mostly of (1) subhedral PL crystals, sometimes slightly to moderately resorbed and often containing glassy melt inclusions, (2) strongly resorbed, anhedral CPX also containing inclusions and deep glassy embayments, (3) small euhedral olivine and Cr-spinel crystals, and (4) interstitial glass. Olivine is present in trace amounts only (< 1 vol%). The volume proportions of clinopyroxene and plagioclase are in the range 38–58% PL, 24–39% CPX; around 13–28% is composed by interstitial groundmass (Table 2). Though clinopyroxene is strongly resorbed in all samples studied, with anhedral shape and porous texture of separate grains (Fig. 2b, c), all individual CPX grains in each thin

Table 1 Precision and accuracy of trace element analyses by SIMS

Elements (ppm)	KL2-G Ref	21–24 October 2002, $N=5$			6–8 December 2002, $N=5$			16–17 December 2002, $N=3$		
		Mean	2RSD	ΔRV	Mean	2RSD	ΔRV	Mean	2RSD	ΔRV
K	4,000	3,816	4.8	−4.6	3,624	3.9	−9.4	3,830	10.4	−4.3
Ti	15,600	15,540	3.4	−0.4	15,400	1.3	−1.3	16,067	4.0	3.0
V	370	262	5.3	−29.2	249	3.2	−32.7	263	5.3	−28.9
Cr	310	298	4.0	−3.9	290	3.4	−6.5	296	2.0	−4.5
Sr	364	398	2.0	9.3	379	1.1	4.1	377	3.2	3.6
Ba	123	137	7.3	11.4	124	3.2	0.8	122	4.9	−0.8
Y	26.8	24.9	4.0	−7.1	24.1	1.7	−10.1	24.4	4.9	−9.0
Zr	159	156	6.4	−1.9	150	2.7	−5.7	156	5.1	−1.9
Nb	15.8	17.7	4.5	12.0	16.2	2.5	2.5	17.2	7.0	8.9
La	13.2	13.5	5.9	2.3	12.8	3.1	−3.0	12.7	3.1	−3.8
Ce	32.9	34.7	6.9	5.5	32.2	4.3	−2.1	32.3	1.9	−1.8
Pr	4.71	5.18	8.5	10.0	4.85	5.8	3.0	4.79	4.6	1.7
Nd	21.7	23	8.7	6.0	21.7	4.6	0.0	21.5	3.7	−0.9
Sm	5.55	6.05	10.9	9.0	5.71	9.5	2.9	5.44	8.1	−2.0
Eu	1.95	2.17	8.3	11.3	2.06	8.7	5.6	1.91	7.3	−2.1
Gd	6.1	5.93	25.0	−2.8	5.58	18.6	−8.5	5.3	7.5	−13.1
Dy	5.35	5.64	7.8	5.4	4.98	8.8	−6.9	4.87	4.9	−9.0
Ho	0.99	1.03	7.8	4.0	0.95	12.6	−4.0	0.89	13.5	−10.1
Er	2.64	2.77	6.5	4.9	2.34	12.0	−11.4	2.44	13.9	−7.6
Yb	2.13	2.21	10.9	3.8	1.88	13.8	−11.7	1.89	15.9	−11.3

Precision and accuracy of trace element analyses were controlled by multiple analyses of KL2-G reference glass during each analytical session

N number of replicates; *REF* reference values of trace element concentrations (given in ppm) of KL2-G from Jochum et al. (2000); *Mean* average value obtained from replicate analyses of KL2-G; *2RSD* (given in %) 2-sigma relative standard deviation obtained during a given analytical session and defined as $100 \times 2\sigma \text{ SD}/\text{Mean}$; *ΔRV* (given in %) deviation from the reference values (over a given analytical session) that characterizes the accuracy of trace element analyses and defined as $100 \times (\text{Mean}/\text{Ref} - 1)$; all analyses of melt inclusions and groundmass glasses (Table 6) were corrected for ΔRV values

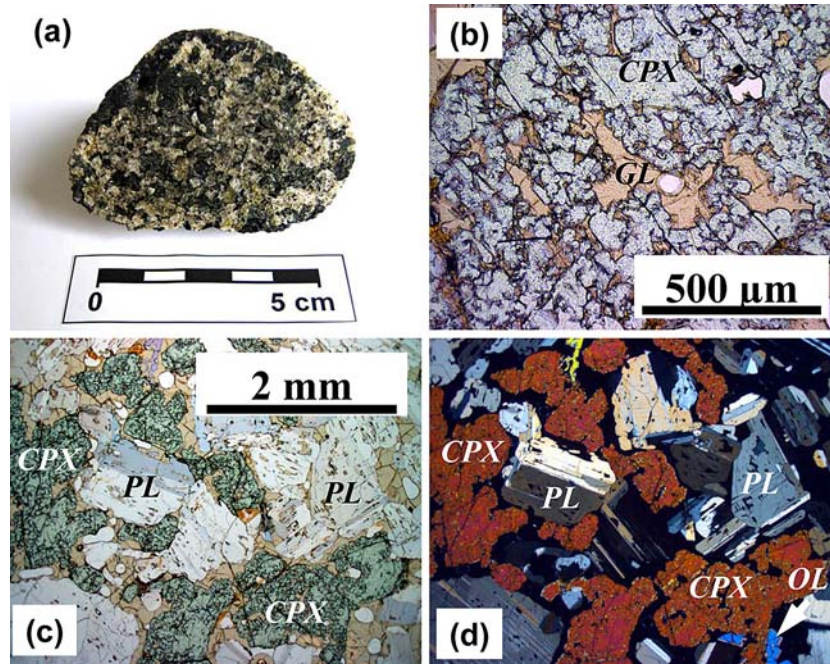


Fig. 2 Photomicrographs showing size and texture of gabbro xenoliths in pillow lavas from Midfell area, SW Iceland. **a** General view of a gabbro xenolith composed mostly of clinopyroxene (*dark-green grains*), plagioclase (*grains having white, gray or beige color*) and containing *dark-brown halo* of quenched glass. **b** Spongy texture of one clinopyroxene grain filled by naturally quenched glass, sample ICS01-8-1; in this panel and panel (c), the *small, white*

rounded blebs are gas vesicles in the interstitial glass presently filled by epoxy resin. **c** Strongly resorbed CPX grains, subhedral PL crystals and interstitial glass demonstrating typical xenolith's texture, sample ICS01-8-1; plane-polarized light. **d** The same field of view as in (c) but given in cross-polarized light showing that all seen CPX grains compose a single oikocryst. OL olivine, CPX clinopyroxene, PL plagioclase, GL glass

section examined are characterized by simultaneous extinction in the cross-polarized light representing individual fragments of the same oikocryst (Fig. 2d). In contrast, plagioclase grains have different crystallographic orientation and are characterized mostly by subhedral crystal shape and are generally less resorbed than clinopyroxene (Fig. 2c, d). The summary of mineral chemistry is given in Table 3, and chemical composition of mineral phases appears to be similar to those described by Risku-Norja (1985).

Deep glassy embayments and inclusions are very common in clinopyroxene and plagioclase. The embayments in CPX, unlike those in PL, form a network inside CPX crystals connecting to interstitial glass. Inclusions are represented by glassy (quenched glass \pm gas bubble) and multiphase (glass \pm daughter crystals \pm gas bubble) types and occur as single, isolated inclusions and randomly oriented groups; inclusions in plagioclase trace often zones of crystal growth. Well-quenched glassy inclusions containing no daughter crystals are more abundant in CPX, while PL preferentially contains partially crystallized inclusions. We analyzed only glassy embayments in CPX and PL; detailed examination of CPX- and PL-hosted melt inclusions is beyond the scope of the present study.

The broad range of PL composition is bracketed between 80.5 and 89.7 mol% of anorthite ($An = 100 \times Ca / (Ca + Na)$, atomic ratio; Table 3). Many PL grains are reversely or oscillatory zoned (Fig. 3a, b).

The compositional difference between cores and rims of the individual PL crystals can reach > 10 mol% An. It is essential to note that crystal rims are systematically more Ca- and Al-rich compared to the cores; similar Ca- and Al-enrichment and Na depletion is observed in the PL rims on the contact with glassy embayments (Fig. 3a, b) implying adjustment of PL composition to the chemical variations of interstitial melt.

Similarly to plagioclase, clinopyroxene shows a wide compositional range; *mg*-number [$mg\#_{cp\#} = 100 \times Mg / (Mg + Fe_{tot})$, atomic ratio, where Fe_{tot} is total iron] ranges from 82.9 to 90.2, concentrations of Ti, Al and Na are 0.2–0.5 wt% TiO_2 , 2.8–5.7 wt% Al_2O_3 , and 0.1–0.3 wt% Na_2O (Fig. 4a, Table 3). Many CPX grains show reverse zoning ($mg\#_{core} = 82–88$, $mg\#_{rim} = 87–90$) but this zonation is not as regular as in PL (Fig. 3c, d). Overall, the outer parts of the grains are significantly more Mg-rich than the cores. The difference in 2–3 mol% of *mg*-number is commonly observed in individual CPX grains; this also can be traced by coherent variations of other components such as Al_2O_3 , (Fig. 3c), TiO_2 and Cr_2O_3 (not shown). Almost all CPX grains have narrow (a few μm) rims showing sharp drop of *mg*-number and probably formed due to rapid quenching of the transporting magma at decreasing T and P . Chemical composition of CPX grains composing the nodules are similar to those from the transporting lavas, as it has been also observed by Risku-Norja (1985; Fig. 4a).

Table 2 Bulk-rock composition of the Midfell gabbro nodules

Sample ^a	ICS01-8-1	ICS01-8-2	ICS01-8-3	ICS01-8-4	ICS01-8-5	ICS01-8-8	ICS01-8-10	Mean Gab	$\pm 1\sigma$	Uncert.	DL
Modal composition (observed) ^b											
OL	<1	<1	<1	<1	<1	<1	<1	<1	–	–	–
CPX	24	41	36	40	27	28	35	33	7	–	–
PL	58	43	50	42	56	52	49	50	6	–	–
SP	<1	<1	<1	<1	<1	<1	<1	<1	–	–	–
GL	18	16	14	19	17	20	16	17	2	–	–
Modal composition (calculated) ^c											
OL	0.6	0.2	0.6	1.8	1.0	1.9	2.2	1.2	0.8	–	–
CPX	30.5	32.2	28.3	28.4	26.7	25.4	27.0	28	2	–	–
PL	54.2	55.8	57.7	49.8	60.9	49.6	53.7	55	4	–	–
SP	2.4	2.5	1.5	1.8	2.1	1.2	2.1	1.9	0.5	–	–
GL	12.2	9.4	11.9	18.3	9.3	22.0	15.0	14	5	–	–
Major elements (wt%) ^d											
SiO ₂	47.47	47.63	47.52	47.17	47.04	47.54	47.34	47.4	0.2	<1	0.2
TiO ₂	0.33	0.28	0.27	0.32	0.29	0.34	0.31	0.31	0.03	<20	0.05
Al ₂ O ₃	21.43	21.68	22.32	20.97	22.83	20.97	21.64	21.7	0.7	<1	0.1
Fe ₂ O ₃	4.65	4.29	3.97	4.71	4.13	4.87	4.63	4.5	0.3	<2	0.1
MnO	0.08	0.06	0.06	0.07	0.06	0.08	0.08	0.07	0.01	<10	0.03
MgO	7.28	7.09	6.61	7.7	6.4	7.54	7.52	7.2	0.5	<1	0.1
CaO	17.73	17.69	17.8	17.52	17.47	17.25	17.35	17.5	0.2	<2	0.1
Na ₂ O	1.16	1.15	1.14	1.06	1.14	1.11	1.08	1.12	0.04	<2	0.05
K ₂ O	BDL	BDL	BDL	BDL	BDL	BDL	BDL	–	–	<10	0.1
P ₂ O ₅	BDL	BDL	BDL	BDL	BDL	BDL	BDL	–	–	<10	0.05
LOI	0.15	0.05	0.23	0.49	0.57	0.44	0.50	0.3	0.2	–	–
Total	100.28	99.92	99.92	100.01	99.93	100.14	100.45	100.1	0.2	–	–
Trace elements (ppm) ^d											
V	140.8	129.1	118.1	138.2	119	144	133	132	10	<5	1.5
Cr	2,108	1,817	1,736	2,936	1,748	2,172	2,761	2,183	488	<5	5
Co	26.6	24.8	22.2	27.9	23.2	27.8	26.9	26	2	<10	0.2
Ni	136	125	109	145	111	139	150	131	16	<10	4
Cu	41.0	35.3	31.5	59.9	34.5	42.7	36.6	40	9	<10	3
Zn	25.3	22.3	19.6	26.3	20.5	25.3	25.0	23	3	<10	8
Sr	149	160	154	138	165	133	140	148	12	<5	2
Y	5.9	5.2	4.8	5.7	5.0	5.8	5.5	5.4	0.4	<5	0.08
Zr	7.1	6.4	6.9	7.5	6.8	7.1	8.1	7.1	0.5	<10	1
Nb	0.27	0.29	0.33	0.28	0.30	0.30	0.28	0.29	0.02	<15	0.07
Ba	6.4	7.0	6.8	7.6	8.7	6.9	7.5	7.3	0.8	<15	3.5
La	0.43	0.44	0.45	0.41	0.49	0.43	0.40	0.44	0.03	<5	0.04
Ce	1.29	1.30	1.26	1.23	1.38	1.30	1.22	1.28	0.05	<10	0.09
Pr	0.23	0.23	0.22	0.22	0.24	0.23	0.22	0.23	0.01	<10	0.01
Nd	1.29	1.30	1.20	1.28	1.29	1.37	1.29	1.29	0.05	<5	0.03
Sm	0.52	0.50	0.46	0.52	0.48	0.56	0.52	0.51	0.03	<10	0.01
Eu	0.29	0.29	0.27	0.29	0.30	0.29	0.28	0.29	0.01	<5	0.01
Gd	0.78	0.73	0.66	0.79	0.71	0.80	0.74	0.74	0.05	<5	0.01
Tb	0.15	0.13	0.12	0.15	0.13	0.14	0.14	0.14	0.01	<5	0.01
Dy	1.00	0.89	0.83	1.00	0.86	1.03	0.96	0.94	0.08	<5	0.02
Ho	0.21	0.19	0.18	0.21	0.19	0.22	0.21	0.20	0.01	<5	0.01
Er	0.62	0.54	0.51	0.60	0.53	0.61	0.58	0.20	0.01	<5	0.01
Yb	0.62	0.54	0.49	0.59	0.53	0.60	0.56	0.56	0.05	<10	0.005
Lu	0.10	0.08	0.08	0.09	0.08	0.09	0.09	0.09	0.01	<10	0.005
[La/Sm] _n	0.52	0.55	0.61	0.49	0.64	0.48	0.48	0.54	0.06	–	–
[Ba/Nb] _n	2.49	2.54	2.17	2.85	3.05	2.42	2.82	2.62	0.30	–	–
[Sr/Sr*] _n	7.74	8.24	8.39	7.37	8.28	6.67	7.47	7.74	0.62	–	–
[Zr/Zr*] _n	0.57	0.52	0.61	0.60	0.57	0.53	0.65	0.58	0.05	–	–

^aLabels starting from ICS are original sample numbers; Mean Gab. and 1σ = gabbro composition given at $\pm 1\sigma$ standard deviation and calculated as an average of bulk-rock composition of individual gabbro nodules; Uncert. = analytical uncertainty given in percent, DL = detection level given in wt% for major elements and in ppm for trace elements, both provided by Analytical Service of Rocks and Minerals (SARM) at the CRPG-CNRS (Nancy, France); for more details, see Carignan et al. (2001)

^bModal composition obtained from computer analysis of digital images. *OL* Olivine, *CPX* Clinopyroxene, *PL* Plagioclase, *SP* spinel, *GL* Glass

^cModal composition obtained from mass–balance calculations using major element compositions of minerals and glasses composing gabbro nodules

^dMajor (wt%) and trace element (ppm) concentrations in whole-rock samples were analyzed by ICP-AES using Analytical Service of Rocks and Minerals at the CRPG-CNRS (Nancy, France) (see text for details); *BDL* Below detection level. In this table and Table 5, [La/Sm]_n and [Ba/Nb]_n are element ratios normalized to chondrite after Anders and Grevesse (1989), [Sr/Sr*]_n and [Zr/Zr*]_n represent magnitudes of Sr and Zr anomalies defined as $[Sr]_n / ([Ce]_n \times [Nd]_n)^{0.5}$ and $[Zr]_n / ([Nd]_n \times [Sm]_n)^{0.5}$, respectively, where subscript *n* points at chondrite-normalized element concentrations

Olivine ($\text{Fo}_{87.2-89.1}$, 0.34–0.44 wt% CaO, 0.20–0.30 wt% NiO; Table 3) from gabbro nodules is indistinguishable from that in the surrounding pillow rim glasses ($\text{Fo}_{85.3-90.2}$, 0.33–0.47 wt% CaO, 0.16–0.37 wt% NiO; Fig. 4b, Table 3).

Spinel microphenocrysts in the surrounding quenched glass and those from the nodules are also very similar in composition (Fig. 4c, Table 3). They correspond well to the reference field of spinel compositions from MORB and Ol-hosted spinel inclusions from Reykjanes and Hengill tholeiitic lavas (Gurenko et al. 1990; Gurenko and Chaussidon 1995) (Fig. 4c). Nearly 40% of the population exceeds the range of SP inclusions in OL from Icelandic tholeiites being slightly more Ti-rich and Mg-poor (Fig. 4c).

Bulk-rock composition of gabbro nodules

Major and trace element concentrations of seven gabbro nodules analyzed are very similar; the observed variations for almost all elements (given as a ratio of 2σ SD to a mean value) are comparable with analytical error. The nodules are slightly depleted in light rare earth elements relative to middle and heavy rare earth elements ($[\text{La}/\text{Sm}]_n = 0.5\text{--}0.6$). They show significant enrichment

of Ba relative to Nb ($[\text{Ba}/\text{Nb}]_n = 2.2\text{--}3.1$), Sr relative to Ce and Nd and depletion of Zr relative to Nd and Sm ($[\text{Sr}/\text{Sr}^*]_n = 6.7\text{--}8.4$, $[\text{Zr}/\text{Zr}^*]_n = 0.52\text{--}0.65$, where $(\text{Sr}/\text{Sr}^*)_n$ and $(\text{Zr}/\text{Zr}^*)_n$ are magnitudes of Sr excess and Zr depletion normalized to chondrite; Table 2). The composition of the Midfell nodules is very similar to that of the oceanic crust gabbro reported by Hart et al. (1999).

Glass compositions

We analyzed different types of glasses associated with the gabbro nodules for major and trace element compositions. These are: (1) chilled glass margins of the host pillow-basalt (HOST-GL), (2) glassy crusts on the xenolith's surface (RIND-GL), (3) interstitial glasses inside gabbro nodules (INT-GL), and (4) deep glassy embayments in nodule-forming CPX and PL grains (CPX-GL and PL-GL, respectively).

Concentrations of major elements and sulfur

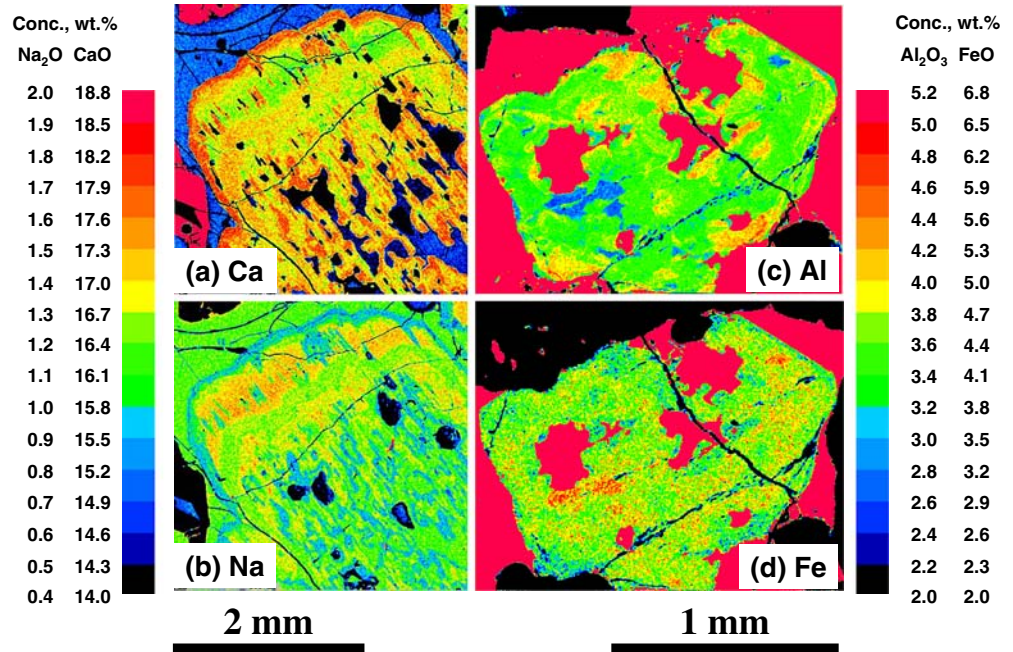
Major element compositions of different glass types associated with gabbro nodules are listed in Tables 4 and 5, and presented in Fig. 5. All Midfell HOST-GLs

Table 3 Summary of mineral chemistry

Sample	ICS01-8-Gl	ICS01-8-1	ICS01-8-2	ICS01-8-4	ICS01-8-5	ICS01-8-6	ICS01-8-8	ICS01-8-13
Olivine								
N	4-Gl	5-Gab	8-Gl	–	13-Gl	17-Gl	18-Gl	10-Gab
Fo	87.3–88.3	88.1–88.5	86.2–87.6	ND	86.7–88.6	86.8–89.7	85.3–90.2	87.2–89.1
CaO	0.36–0.42	0.39–0.43	0.34–0.45	ND	0.33–0.47	0.34–0.45	0.33–0.44	0.34–0.44
NiO	0.22–0.23	0.21–0.26	0.20–0.22	ND	0.22–0.31	0.21–0.31	0.16–0.37	0.20–0.30
Clinopyroxene								
N	–	24-Gab	15-Gab	31-Gab	52-Gab	33-Gab	22-Gab	35-Gab
mg# _{cp}	ND	85.9–90.2	86.6–87.8	86.2–89.5	85.3–88.6	84.8–89.7	82.9–88.1	85.4–88.7
TiO ₂	ND	0.21–0.46	0.25–0.32	0.22–0.33	0.25–0.43	0.21–0.51	0.21–0.42	0.22–0.36
Al ₂ O ₃	ND	2.8–5.7	3.9–4.3	3.8–5.3	3.2–5.0	3.0–4.4	3.9–4.8	3.2–5.3
CaO	ND	19.9–21.6	20.8–21.1	20.4–21.7	20.5–21.5	20.7–21.8	20.0–21.5	20.7–21.9
Na ₂ O	ND	0.15–0.27	0.19–0.27	0.16–0.29	0.18–0.27	0.14–0.23	0.20–0.31	0.15–0.24
Plagioclase								
N	1	27-Gab	15-Gab	9-Gab	25-Gab	18-Gab	36-Gab	40-Gab
An	88.7	80.5–89.3	80.5–88.9	81.6–89.7	83.2–89.1	84.0–89.0	81.5–89.6	83.7–89.3
K ₂ O	0.02	0.00–0.03	0.00–0.02	0.00–0.02	0.00–0.03	0.00–0.02	0.00–0.03	0.00–0.03
Spinel								
N	–	5-Gab	12-Gab	7-Gab	5-Gab	12-Gab	2-Gab	–
mg# _{sp}	ND	66.4–68.5	67.4–72.8	67.1–73.6	67.0–68.0	66.1–69.9	70.4–70.8	ND
cr# _{sp}	ND	43.8–50.6	28.9–48.3	33.4–50.0	51.6–57.9	40.3–51.3	47.4–49.4	ND
TiO ₂	ND	0.42–0.54	0.30–0.40	0.28–0.49	0.35–0.40	0.29–0.49	0.31–0.36	ND
Fe ²⁺ /Fe ³⁺	ND	1.6–1.8	1.6–2.1	1.8–2.1	2.0–2.2	1.9–2.1	1.9–2.0	ND
N	35-Gl	6-Gl	3-Gl	–	13-Gl	14-Gl	19-Gl	17-Gl
mg# _{sp}	65.2–73.6	66.5–72.4	66.5–72.4	ND	64.3–72.1	65.7–72.1	69.0–72.8	67.8–72.9
cr# _{sp}	30.3–59.6	38.3–46.4	36.8–46.4	ND	28.8–49.1	29.1–52.9	34.4–49.9	28.7–45.8
TiO ₂	0.21–0.52	0.28–0.47	0.28–0.50	ND	0.23–0.56	0.28–0.55	0.23–0.41	0.26–0.44
Fe ²⁺ /Fe ³⁺	1.5–2.4	1.9–2.4	1.7–2.4	ND	1.7–2.7	1.7–2.1	1.7–2.4	1.7–2.1

Individual analyses are available on request; *N* number of microprobe analyses (*Gl* analyzed in host pillow rim glass, *Gab* analyzed inside gabbro nodules), *Fo* mol% forsterite in olivine, $\text{mg}\#_{\text{cp}} = 100 \times \text{Mg}/(\text{Mg} + \text{Fe}_{\text{tot}})$, atomic ratio, where Fe_{tot} is a total iron as FeO; *An* mol% anorthite, $\text{mg}\#_{\text{sp}} = 100 \times \text{Mg}/(\text{Mg} + \text{Fe}^{2+})$, atomic ratio, where Fe^{2+} was calculated on the basis of spinel stoichiometry; *cr#_{sp}* spinel *cr*-number, $100 \times \text{Cr}/(\text{Cr} + \text{Al})$, atomic ratio; TiO₂, Al₂O₃, CaO, NiO, Na₂O and K₂O contents are given in wt%; ND Not determined; – Phase is not present or not analyzed

Fig. 3 Typical element distribution in plagioclase and clinopyroxene composing gabbro nodules. (a, b) Fragment of one oscillatory zoned plagioclase crystal, sample ICS01-8-4, (a) *Ca*, (b) *Na*; (c, d) clinopyroxene, sample ICS01-8-13, (c) *Al*, (d) *Fe*



containing gabbro nodules are tholeiitic basalts. They are characterized by narrow compositional variations within a given lava sequence, and correspond to the Icelandic tholeiitic rocks and glasses (Fig. 5, Table 4).

The compositions of HOST-GLs having no contact with gabbro nodules are similar to those located directly around the nodules (i.e., RIND-GL; Fig. 5). The concentrations of sulfur are generally low, ranging from

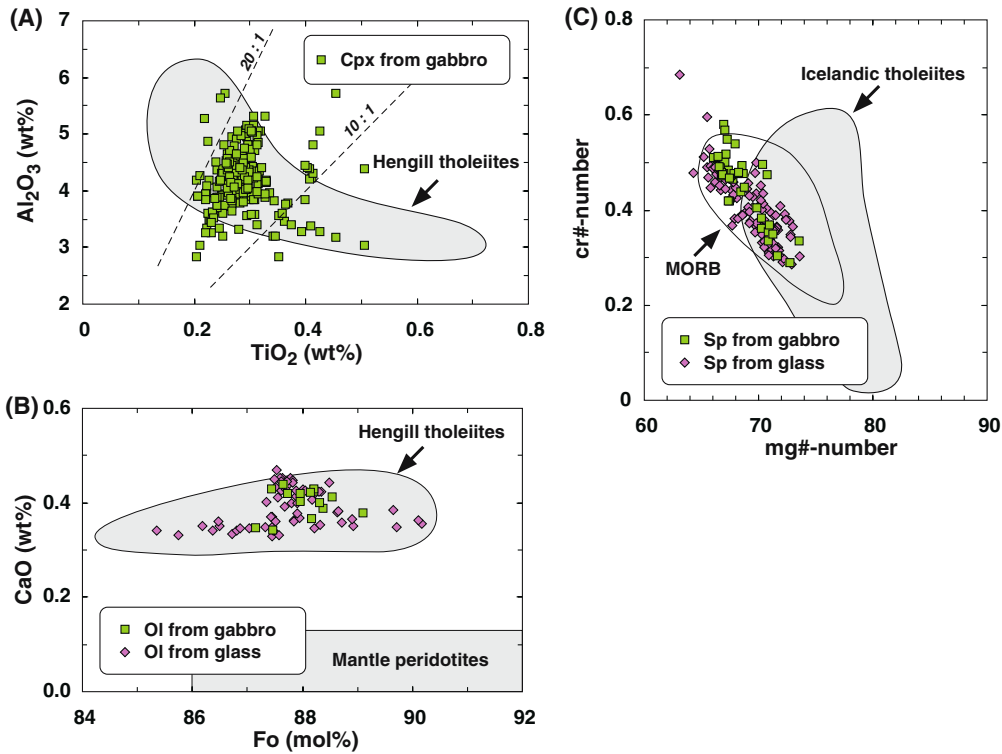


Fig. 4 Olivine, clinopyroxene and spinel compositions. **a** Al₂O₃ versus TiO₂ contents in clinopyroxene. **b** CaO versus Fo contents in olivine. **c** *cr*-number versus *mg*-number in spinel from gabbro nodules and host matrix glasses given in comparison with the

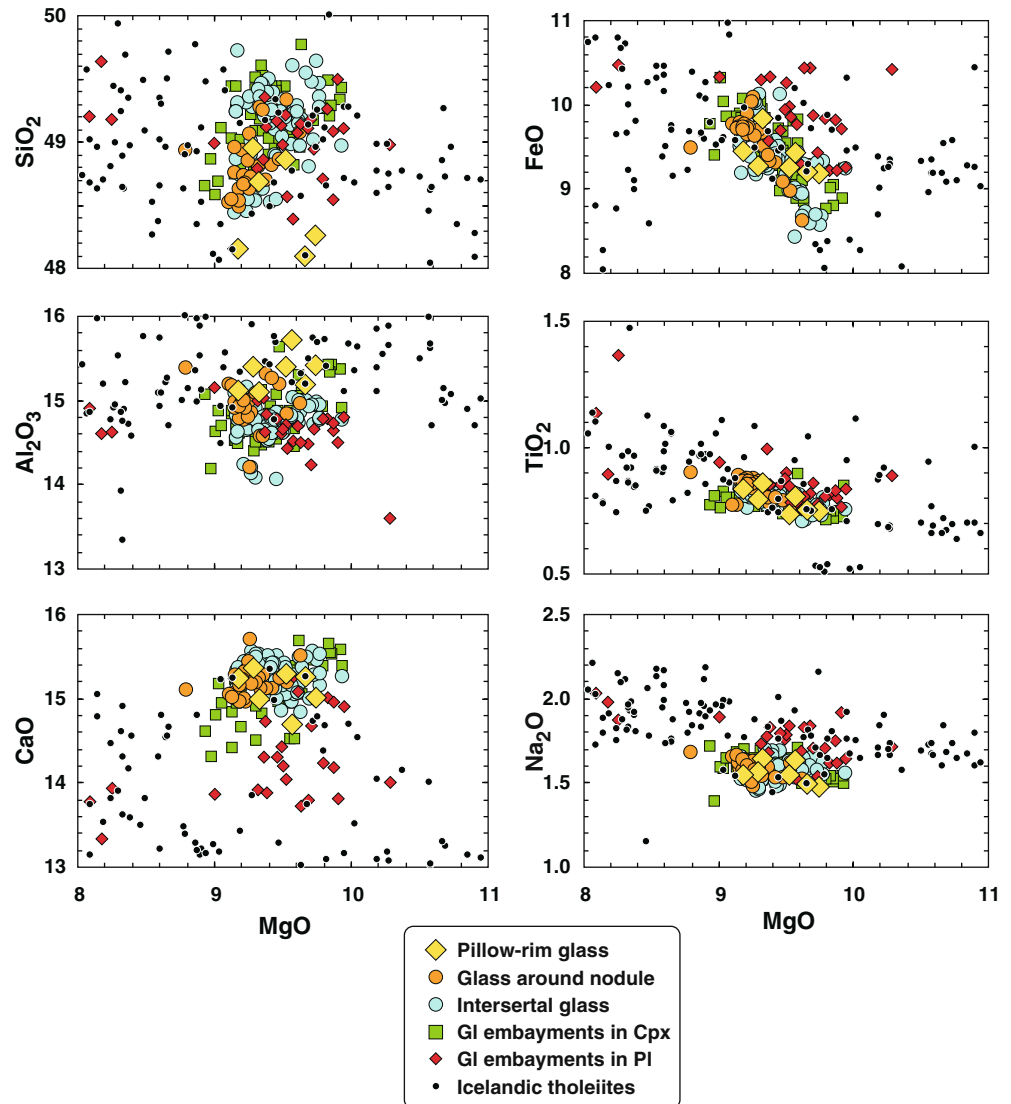
mineral composition of the Icelandic tholeiites. Reference fields represent data from Gurenko et al. (1990), Gurenko and Chaussidon (1995) and author's unpublished data

Table 4 (Contd.)

Sample	SiO ₂	TiO ₂	Al ₂ O ₃	FeO	MnO	MgO	CaO	Na ₂ O	K ₂ O	P ₂ O ₅	Total	S	K ₂ O/TiO ₂	CaO/Al ₂ O ₃	<i>P</i> _{calc}	<i>T</i> _{calc}	Fo _{equil}	mg# _{equil}
ICS01-8-8b (2)	49.47	0.75	14.94	8.68	0.15	9.74	15.54	1.53	0.03	0.03	100.85	0.031	0.04	1.04	50	1,217	88.0	89.2
1σ	0.00	0.02	0.01	0.01	0.01	0.02	0.02	0.01	0.00	0.01	–	0.003	–	–	20	0	0.1	0.0
ICS01-8-8c (3)	49.59	0.77	15.01	8.53	0.15	9.67	15.41	1.55	0.04	0.03	100.73	0.037	0.05	1.03	40	1215	88.0	89.3
1σ	0.05	0.02	0.03	0.09	0.01	0.09	0.11	0.05	0.00	0.02	–	0.007	–	–	20	2	0.0	0.1
ICS01-8-8e (2)	49.17	0.71	14.99	8.70	0.16	9.63	15.43	1.56	0.03	0.03	100.40	0.037	0.04	1.03	50	1,215	87.8	89.0
1σ	0.01	0.01	0.01	0.02	0.01	0.01	0.07	0.01	0.01	0.00	–	0.003	–	–	20	0	0.0	0.0
ICS01-8-13a (1)	49.31	0.87	14.76	9.73	0.18	9.17	15.23	1.58	0.03	0.02	100.88	0.039	0.03	1.03	–30	1,200	85.8	87.2
ICS01-8-13b (3)	49.32	0.83	14.55	9.51	0.17	9.24	15.20	1.61	0.04	0.04	100.51	0.037	0.04	1.04	–20	1,203	86.2	87.6
1σ	0.15	0.02	0.01	0.04	0.01	0.14	0.13	0.02	0.00	0.01	–	0.005	–	–	50	4	0.2	0.2
ICS01-8-13c (2)	49.34	0.81	14.57	9.37	0.15	9.40	15.10	1.67	0.05	0.03	100.51	0.036	0.06	1.04	50	1212	86.6	88.0
1σ	0.02	0.01	0.05	0.03	0.00	0.00	0.01	0.02	0.00	0.01	–	0.003	–	–	0	0	0.0	0.0
ICS01-8-13d (1)	49.45	0.81	14.59	9.42	0.17	9.36	15.20	1.64	0.05	0.06	100.74	0.034	0.06	1.04	10	1,208	86.5	87.9
ICS01-8-13e (1)	49.41	0.82	14.66	9.52	0.16	9.35	15.10	1.69	0.04	0.04	100.79	0.036	0.05	1.03	40	1,209	86.4	87.7

Average chemical compositions calculated from individual glass analyses (a number of analyses is given in brackets), each of which represent an average of three to five points of electron microprobe analyses; 1σ = 1-sigma standard deviation calculated for three and more analyses and indicates a deviation from the average in the case of two measurements; P_{calc} and T_{calc} = pressure (MPa) and temperature (°C) calculated using empirical olivine–melt and clinopyroxene–melt geothermometers (Ford et al. 1983; Danyushevsky 2001 and references therein) and the method suggested by Danyushevsky et al. (1996), while Fo_{equil} (mol%) and mg#_{equil} (atomic %) are calculated equilibrium compositions of olivine and clinopyroxene, respectively. – no value

Fig. 5 MgO variation diagrams presenting major element composition of different glass types from Midfell gabbro nodules. In this figure and Figs 6, 7, 10, Icelandic tholeiites are compositions of the Icelandic tholeiitic rocks and glasses taken from GEOROC database (URL: <http://www.georoc.mpch-mainz.gwdg.de/georoc>) and author's unpublished data



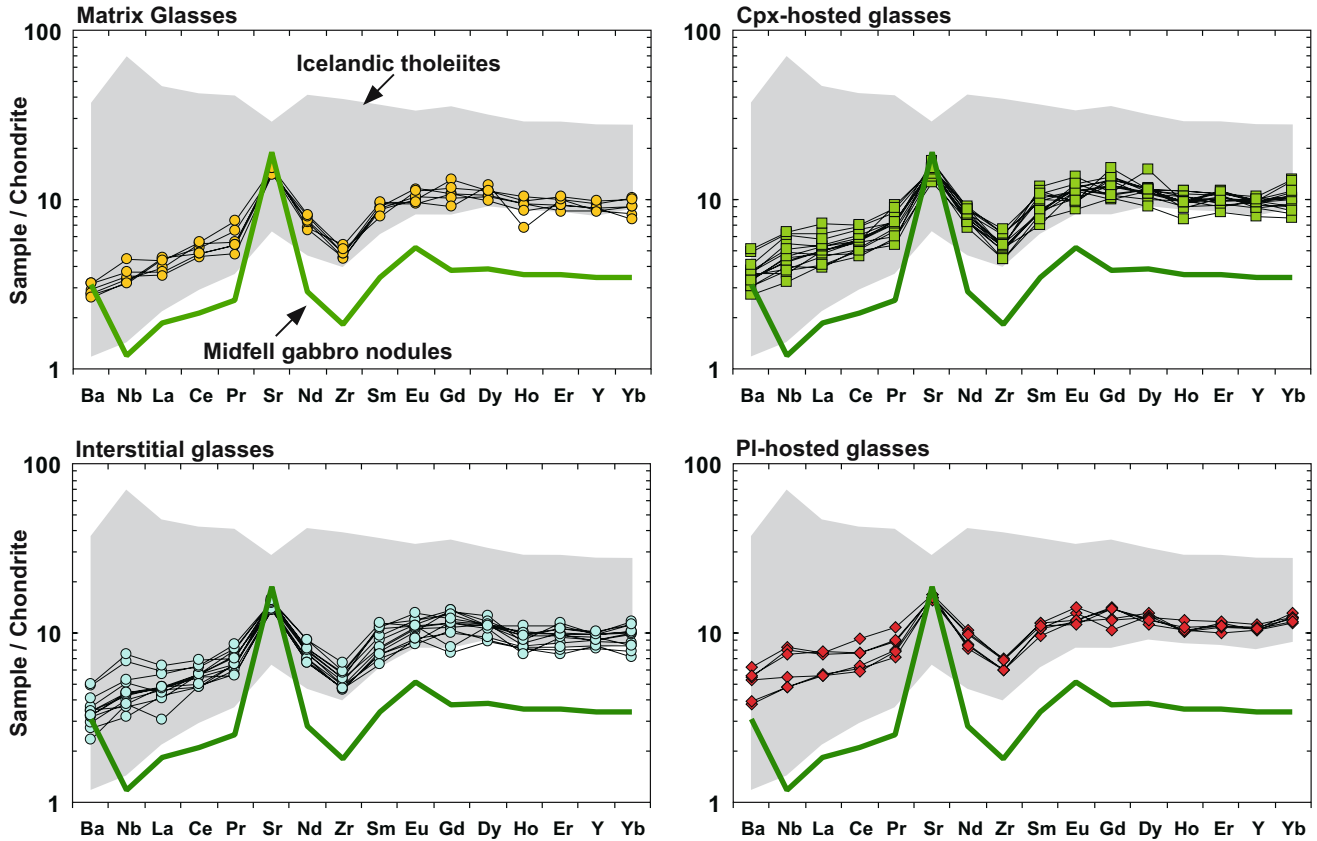


Fig. 6 Trace elements in the glasses associated with gabbro nodules. Average bulk-rock composition of the Midfell gabbro nodules is given for comparison. Data source for Icelandic

tholeiites are similar as pointed in Fig. 5. Chondrite normalizing values are taken from Anders and Grevesse (1989)

130–450 ppm S in HOST-GL and RIND-GL to 230–580 ppm S in INT-GL and CPX-GL but increasing up to 1,200 ppm S in PL-GL (Tables 4, 5). No correlation of S contents with FeO is observed.

No essential difference with respect to major elements between host pillow-rim glasses (both HOST-GL and RIND-GL types; $K_2O/TiO_2=0.02\text{--}0.04$, $CaO/Al_2O_3=0.93\text{--}1.04$) and INT-GL ($K_2O/TiO_2=0.03\text{--}0.06$, $CaO/Al_2O_3=1.00\text{--}1.07$) was recognized. The CPX-GL ($K_2O/TiO_2=0.02\text{--}0.06$, $CaO/Al_2O_3=1.00\text{--}1.06$) have chemical compositions very close to those of HOST-GL and RIND-GL. It has to be noted, however, that RIND-GL, HOST-GL and CPX-GL are located at the lower end of the Al_2O_3 range but show systematically higher CaO contents, as compared to the Icelandic rocks and glasses (Fig. 5). The PL-GL ($K_2O/TiO_2=0.03\text{--}0.11$, $CaO/Al_2O_3=0.87\text{--}1.06$), though overlapping with other glass types, are characterized by somewhat lower CaO and higher FeO, and Na_2O contents at a given MgO content (Fig. 5) and vary more significantly in CaO/Al_2O_3 ratios (not shown). We ascribe these differences to more extended post-entrapment crystallization of melt portions enclosed in plagioclase since small daughter crystals are often observed on the inclusion walls, whereas CPX-GL in most cases are crystal-free.

Trace elements

The chondrite-normalized trace element spectra of the different glass types are given in Table 6 and shown in Fig. 6 together with bulk-rock compositions of gabbro xenoliths (Table 3); the compositions of tholeiitic rocks and glasses collected within the neovolcanic rift zone of Iceland (GEOROC database and author's unpublished data) are given for comparison. The Midfell glasses are characterized by the most extensive Sr enrichment and Zr depletion ($[Sr/Sr^*]_n=1.7\text{--}2.7$; $[Zr/Zr^*]_n=0.56\text{--}0.71$; Fig. 7), as compared to the Icelandic tholeiites in general. Furthermore, all “nodule-related” glasses studied show overall depletion in Ba relative to Nb ($[Ba/Nb]_n=0.45\text{--}0.96$), whereas the bulk-rock analyses of their host gabbro xenoliths demonstrate a prominent Ba enrichment ($[Ba/Nb]_n=2.2\text{--}3.1$; Table 2, Fig. 6).

Pressure and temperature conditions of xenolith's origin

Olivine and CPX are the most common phenocrysts in the nodule-transporting magmas; CPX is also a main rock-forming mineral of the gabbro nodules. Though OL is less abundant in the gabbro xenoliths studied but being described in the other types of the Midfell

Table 5 Major element composition and S concentrations of glassy embayments, and their host clinopyroxenes and plagioclases from Midfell gabbro nodules

Sample	Phase ^a	SiO ₂	TiO ₂	Al ₂ O ₃	Cr ₂ O ₃	FeO	MnO	MgO	CaO	Na ₂ O	K ₂ O	P ₂ O ₅	Total	S	mg#,An	K ₂ O/TiO ₂	CaO/Al ₂ O ₃	<i>P</i> _{calc}	<i>T</i> _{calc}
ICS01-8-1																			
181a-c1g1	Emb	48.65	0.80	14.46	ND	9.84	0.18	9.34	15.34	1.56	0.02	0.02	100.22	0.031	62.9	0.03	1.06	20	1,211
	CPX	51.96	0.23	3.54	0.98	3.79	0.08	17.67	21.20	0.18	BDL	ND	99.62	ND	89.3	–	–	280	–
181b-c2g1	Emb	48.69	0.83	14.86	ND	10.02	0.17	9.04	15.16	1.59	0.02	0.04	100.42	0.034	61.6	0.03	1.02	–10	1,201
	CPX	51.45	0.22	3.95	1.35	3.95	0.08	17.28	21.16	0.18	BDL	ND	99.64	ND	88.6	–	–	320	–
181d-c4g1	Emb	48.68	0.80	14.50	ND	9.94	0.17	9.32	15.41	1.51	0.02	0.03	100.40	0.031	62.6	0.03	1.06	0	1,209
	CPX	51.89	0.24	3.79	1.03	3.66	0.09	17.49	21.47	0.15	BDL	ND	99.83	ND	89.5	–	–	300	–
181e-c5g2	Emb	48.82	0.82	14.40	ND	9.88	0.16	9.29	15.31	1.58	0.02	0.03	100.31	0.033	62.6	0.03	1.06	0	1,209
	CPX	51.54	0.21	4.18	1.20	3.86	0.11	17.66	21.00	0.18	0.01	ND	99.93	ND	89.1	–	–	380	–
181a-pl1g1	Emb	48.79	0.87	14.99	ND	10.29	0.16	9.31	13.91	1.74	0.04	0.05	100.15	0.051	61.7	0.05	0.93	–	–
	PL	45.83	0.05	33.16	BDL	0.56	0.01	0.24	17.80	1.29	0.01	ND	98.94	ND	88.4	–	–	–	–
181b-p2g1	Emb	48.39	0.79	14.53	ND	9.76	0.17	9.57	15.26	1.52	0.03	0.04	100.05	0.051	63.6	0.03	1.05	–	–
	PL	45.66	0.01	32.83	0.02	0.74	BDL	0.22	17.61	1.17	0.01	ND	98.27	ND	89.3	–	–	–	–
181c-p4g1	Emb	48.54	0.83	14.73	ND	9.82	0.17	9.86	14.18	1.75	0.04	0.05	99.97	0.036	64.2	0.05	0.96	–	–
	PL	45.84	0.03	32.98	ND	0.50	0.02	0.21	17.73	1.25	0.01	ND	98.57	ND	88.7	–	–	–	–
181d-p5g1	Emb	48.56	0.78	14.43	ND	9.86	0.17	9.53	15.26	1.58	0.03	0.04	100.24	0.033	63.3	0.03	1.06	–	–
	PL	45.97	0.02	33.02	ND	0.47	0.01	0.24	17.63	1.27	BDL	ND	98.62	ND	88.5	–	–	–	–
ICS01-8-2																			
182a-c1g1	Emb	48.78	0.85	14.85	ND	9.69	0.18	9.20	15.04	1.60	0.03	0.02	100.24	0.025	62.8	0.03	1.01	40	1,209
	CPX	51.43	0.28	4.25	1.05	4.49	0.10	17.02	20.93	0.22	BDL	ND	99.78	ND	87.1	–	–	340	–
182b-c4g1	Emb	48.96	0.86	14.72	ND	9.77	0.17	9.17	15.03	1.67	0.03	0.02	100.39	0.030	62.6	0.03	1.02	30	1,208
	CPX	51.75	0.30	4.14	0.84	4.69	0.12	17.20	20.95	0.24	BDL	ND	100.24	ND	86.7	–	–	330	–
182c-c5g1	Emb	48.99	0.83	14.70	ND	9.53	0.17	9.50	15.15	1.60	0.02	0.03	100.52	0.031	64.0	0.03	1.03	80	1,218
	CPX	52.04	0.27	3.96	0.74	4.56	0.11	17.25	20.93	0.22	BDL	ND	100.09	ND	87.1	–	–	320	–
ICS01-8-4																			
184a-c1g1	Emb	49.22	0.79	14.80	ND	9.58	0.16	9.38	15.12	1.61	0.03	0.01	100.68	0.027	63.6	0.03	1.02	50	1,213
	CPX	50.54	0.31	5.06	1.29	4.46	0.11	16.53	20.89	0.25	0.01	ND	99.44	ND	86.9	–	–	470	–
184a-c1g2	Emb	49.34	0.79	14.81	ND	9.27	0.17	9.42	15.40	1.61	0.03	0.04	100.89	0.033	64.4	0.04	1.04	10	1,211
	CPX	50.61	0.30	5.08	1.32	4.48	0.11	16.57	20.65	0.25	0.01	ND	99.36	ND	86.8	–	–	80	–
184b-c1g1	Emb	49.43	0.79	14.83	ND	9.82	0.16	9.13	14.84	1.59	0.02	0.05	100.66	0.024	62.4	0.03	1.00	0	1,204
	CPX	50.49	0.27	4.94	1.64	4.16	0.10	16.59	21.07	0.24	BDL	ND	99.51	ND	87.7	–	–	430	–
184b-pl1g1	Emb	49.25	0.81	14.77	ND	9.22	0.16	9.83	15.00	1.62	0.03	0.03	100.74	0.034	65.5	0.04	1.02	–	–
	PL	46.75	0.02	32.53	ND	0.48	0.02	0.27	17.04	1.66	0.01	ND	98.77	ND	85.0	–	–	–	–
184b-pl1g2	Emb	49.08	0.80	14.65	ND	9.22	0.17	9.87	14.96	1.62	0.03	0.01	100.41	0.033	65.6	0.04	1.02	–	–
	PL	46.40	0.03	32.60	ND	0.49	0.02	0.25	17.24	1.55	0.01	ND	98.60	ND	86.0	–	–	–	–
184b-pl1g3	Emb	49.11	0.83	14.80	ND	9.26	0.17	9.94	14.91	1.65	0.03	0.03	100.73	0.028	65.7	0.04	1.01	–	–
	PL	45.51	0.01	33.39	ND	0.50	BDL	0.21	17.87	1.18	0.01	ND	98.68	ND	89.3	–	–	–	–
ICS01-8-5																			
185a-c2g1	Emb	49.31	0.82	14.66	ND	9.21	0.18	9.48	15.15	1.56	0.03	0.03	100.43	0.033	64.7	0.03	1.03	40	1,215
	CPX	51.13	0.29	4.46	0.83	4.61	0.12	16.85	20.93	0.24	0.01	ND	99.46	ND	86.7	–	–	380	–
185c-c1g1	Emb	49.25	0.79	14.81	ND	9.11	0.16	9.54	14.94	1.65	0.05	0.04	100.33	0.041	65.1	0.06	1.01	110	1,222
	CPX	51.49	0.29	4.21	0.94	4.65	0.11	16.97	20.85	0.20	0.01	ND	99.71	ND	86.7	–	–	350	–
185e-c1g1	Emb	49.24	0.76	14.83	ND	9.03	0.15	9.50	15.10	1.59	0.05	0.03	100.27	0.037	65.2	0.06	1.02	60	1,218
	CPX	51.57	0.29	3.98	0.78	4.75	0.11	17.05	20.85	0.24	0.01	ND	99.63	ND	86.5	–	–	320	–
185b-pl1g1	Emb	49.20	1.14	14.90	ND	10.21	0.18	8.09	13.78	2.03	0.12	0.08	99.73	0.101	58.5	0.10	0.92	–	–
	PL	45.86	0.03	33.04	ND	0.63	0.01	0.20	17.36	1.37	0.01	ND	98.52	ND	87.4	–	–	–	–
185c-pl1g2	Emb	48.99	0.94	15.15	ND	10.33	0.18	9.00	13.87	1.89	0.05	0.05	100.45	0.048	60.8	0.06	0.92	–	–
	PL	45.92	0.01	32.87	ND	0.50	BDL	0.20	17.58	1.32	0.01	ND	98.41	ND	88.0	–	–	–	–
185d-pl1g1	Emb	48.62	2.14	14.94	ND	11.04	0.19	6.76	13.74	2.12	0.18	0.28	100.01	0.115	52.2	0.08	0.92	–	–
	PL	46.67	0.04	32.49	ND	0.60	0.01	0.20	17.03	1.65	0.02	ND	98.70	ND	85.0	–	–	–	–
ICS01-8-6																			
186a-c1g1	Emb	49.52	0.76	14.62	ND	9.35	0.18	9.36	15.36	1.57	0.03	0.05	100.80	0.037	64.1	0.04	1.05	–30	1,207
	CPX	51.54	0.25	3.68	1.40	3.71	0.09	17.08	21.56	0.17	0.01	ND	99.49	ND	89.1	–	–	270	–
186b-c1g1	Emb	49.10	0.80	14.69	ND	9.86	0.19	9.05	14.95	1.64	0.03	0.03	100.33	0.028	62.1	0.03	1.02	–10	1,203
	CPX	51.92	0.22	3.33	1.09	3.70	0.10	17.29	21.66	0.15	BDL	ND	99.47	ND	89.3	–	–	220	–
186c-c1g1	Emb	49.31	0.82	14.62	ND	9.41	0.17	9.35	15.34	1.58	0.02	0.03	100.65	0.037	63.9	0.03	1.05	–20	1,208
	CPX	51.73	0.22	3.58	1.26	3.70	0.08	17.14	21.53	0.17	BDL	ND	99.43	ND	89.2	–	–	270	–
186d-c1g1	Emb	49.31	0.79	14.61	ND	9.42	0.16	9.39	15.35	1.52	0.03	0.02	100.59	0.031	64.0	0.03	1.05	–20	1,209
	CPX	51.45	0.24	3.87	1.19	3.68	0.09	17.18	21.33	0.15	BDL	ND	99.19	ND	89.3	–	–	300	–
186e-c1g1	Emb	49.10	0.78	14.67	ND	9.54	0.15	9.59	15.11	1.59	0.03	0.03	100.59	0.038	64.2	0.04	1.03	100	1,221
	CPX	51.92	0.23	3.44	1.01	3.60	0.10	17.53	21.34	0.15	BDL	ND	99.32	ND	89.7	–	–	330	–
186d-pl1g1	Emb	49.02	1.46	14.90	ND	11.78	0.21	6.62	13.89	2.08	0.16	0.15	100.27	0.097	50.0	0.11	0.93	–	–
	PL	46.79	0.03	32.17	ND	0.64	0.01	0.19	16.88	1.72	0.02	ND	98.44	ND	84.3	–	–	–	–
186d-pl1g2	Emb	48.86	1.00	15.04	ND	9.83	0.18	9.36	14.30	1.78	0.05	0.10	100.48	0.048	62.9	0.05	0.95	–	–
	PL	46.81	0.02	32.18	ND	0.57	0.01	0.26	17.03	1.64	0.01	ND	98.53	ND	85.1	–	–	–	–

Table 5 (Contd.)

Sample	Phase ^a	SiO ₂	TiO ₂	Al ₂ O ₃	Cr ₂ O ₃	FeO	MnO	MgO	CaO	Na ₂ O	K ₂ O	P ₂ O ₅	Total	S	mg#,An	K ₂ O/TiO ₂	CaO/Al ₂ O ₃	<i>P</i> _{calc}	<i>T</i> _{calc}
ICS01-8-8																			
188a-c1g1	Emb	49.42	0.85	14.90	ND	9.23	0.15	9.94	15.39	1.49	0.02	0.06	101.44	0.037	65.7	0.02	1.03	130	1,228
	CPX	51.03	0.29	4.74	1.33	4.76	0.07	16.46	21.31	0.25	BDL	ND	100.24	ND	86.0	–	–	330	–
188b-c2g1	Emb	49.17	0.75	14.93	ND	8.69	0.16	9.73	15.45	1.50	0.03	0.02	100.43	0.036	66.6	0.04	1.03	60	1,221
	CPX	51.25	0.31	4.24	0.94	5.30	0.13	16.93	20.54	0.25	BDL	ND	99.89	ND	85.1	–	–	320	–
188c-c3g1	Emb	49.44	0.79	15.07	ND	8.96	0.16	9.45	15.13	1.54	0.03	0.01	100.59	0.041	65.3	0.04	1.00	40	1,213
	CPX	51.23	0.30	4.58	1.01	4.74	0.13	17.08	20.92	0.24	BDL	ND	100.21	ND	86.5	–	–	370	–
188d-c4g1	Emb	49.21	0.76	15.05	ND	8.85	0.17	9.63	15.45	1.55	0.03	0.04	100.74	0.034	66.0	0.04	1.03	60	1,218
	CPX	51.98	0.30	4.01	0.70	4.80	0.12	17.30	20.81	0.22	0.01	ND	100.24	ND	86.5	–	–	350	–
188e-c5g1	Emb	48.81	0.78	14.83	ND	8.95	0.16	9.59	15.33	1.54	0.04	0.02	100.04	0.054	65.6	0.05	1.03	70	1,220
	CPX	51.11	0.40	4.44	0.74	6.08	0.20	16.94	20.04	0.31	BDL	ND	100.26	ND	83.2	–	–	330	–
188a-p1g1	Emb	48.94	0.78	14.65	ND	9.42	0.15	9.73	14.98	1.54	0.03	0.03	100.25	0.035	64.8	0.04	1.02	–	–
	PL	45.47	0.02	33.34	ND	0.55	0.01	0.23	17.65	1.12	0.01	ND	98.41	ND	89.6	–	–	–	–
188c-p3g1	Emb	48.56	1.42	15.51	ND	10.88	0.20	7.72	13.54	2.15	0.12	0.15	100.26	0.052	55.8	0.09	0.87	–	–
	PL	46.38	0.03	32.84	ND	0.54	BDL	0.20	17.13	1.55	0.02	ND	98.68	ND	85.9	–	–	–	–
188c-p4g2	Emb	49.63	0.90	14.61	ND	11.20	0.19	8.17	13.33	1.98	0.09	0.04	100.13	0.057	56.5	0.10	0.91	–	–
	PL	46.47	0.02	33.00	0.03	0.54	BDL	0.21	17.14	1.55	0.01	ND	98.97	ND	85.9	–	–	–	–
ICS01-8-13																			
1813a-c1g1	Emb	49.24	0.88	14.53	ND	9.84	0.16	9.17	15.18	1.65	0.03	0.02	100.69	0.035	62.4	0.03	1.05	–10	1,205
	CPX	51.54	0.26	3.74	0.95	4.27	0.11	17.15	21.36	0.19	BDL	ND	99.56	ND	87.7	–	–	260	–
1813a-c1g2	Emb	49.25	0.87	14.48	ND	9.63	0.18	9.17	15.34	1.55	0.03	0.04	100.55	0.034	62.9	0.03	1.06	–70	1,201
	CPX	51.00	0.26	4.36	1.32	4.16	0.09	16.73	21.26	0.21	BDL	ND	99.39	ND	87.8	–	–	350	–
1813b-c2g1	Emb	49.14	0.83	14.51	ND	9.55	0.18	9.41	15.08	1.60	0.04	0.02	100.36	0.043	63.7	0.05	1.04	50	1,215
	CPX	51.02	0.24	4.51	1.13	4.20	0.10	16.90	20.97	0.19	BDL	ND	99.25	ND	87.8	–	–	380	–
1813b-c3g1	Emb	49.40	0.81	14.54	ND	9.48	0.16	9.46	15.14	1.58	0.04	0.04	100.65	0.034	64.0	0.05	1.04	30	1,214
	CPX	51.10	0.26	4.39	1.12	4.36	0.12	16.78	20.93	0.23	0.01	ND	99.29	ND	87.3	–	–	380	–
1813c-c1g1	Emb	49.35	0.80	14.59	ND	9.58	0.18	9.38	15.08	1.62	0.04	0.04	100.64	0.038	63.6	0.05	1.03	40	1,213
	CPX	50.97	0.29	4.48	1.12	4.37	0.11	16.91	20.98	0.22	0.01	ND	99.46	ND	87.3	–	–	380	–
1813d-c4g1	Emb	49.44	0.81	14.66	ND	9.76	0.17	9.16	14.94	1.66	0.04	0.05	100.68	0.036	62.6	0.05	1.02	10	1,206
	CPX	51.03	0.29	4.35	1.17	4.39	0.10	16.76	20.93	0.23	BDL	ND	99.25	ND	87.2	–	–	360	–
1813a-p1g1	Emb	49.41	0.98	14.15	ND	10.14	0.18	9.99	13.65	1.72	0.05	0.06	100.32	0.078	63.7	0.05	0.97	–	–
	PL	45.64	0.02	33.31	ND	0.51	BDL	0.23	17.76	1.22	0.01	ND	98.71	ND	88.9	–	–	–	–
1813e-p1g1	Emb	49.12	0.87	14.63	ND	9.69	0.18	9.46	14.81	1.68	0.05	0.04	100.52	0.043	63.5	0.06	1.01	–	–
	PL	46.32	0.01	32.92	ND	0.54	0.01	0.24	17.25	1.42	0.01	ND	98.72	ND	87.0	–	–	–	–
1813e-p1g2	Emb	49.21	0.86	14.64	ND	9.61	0.17	9.51	14.79	1.68	0.04	0.05	100.56	0.037	63.8	0.05	1.01	–	–
	PL	45.69	0.02	33.31	ND	0.47	0.02	0.21	17.79	1.18	0.01	ND	98.69	ND	89.3	–	–	–	–

Concentrations of major elements were analyzed using the electron microprobe JEOL Superprobe JXA-8200 at the MPI for Chemistry in Mainz (Germany). mg#, An = composition of host mineral; mg# = 100×Mg/(Mg + Fe) of host clinopyroxene given in atomic concentrations, where Fe = total Fe; An = mol% anorthite of host plagioclase, *P*_{calc} = pressure (MPa) calculated using glass compositions and the method of Danyushevsky et al. (1996) (given in lines of glass compositions) and the model of Nimis (1995) for clinopyroxenes (given in lines of clinopyroxene compositions); *T*_{calc} = temperature (°C) calculated using empirical olivine–melt and clinopyroxene–melt geothermometers (Ford et al. 1983; Danyushevsky 2001 and references therein) and the program PETROLOG (Danyushevsky 2001). *ND* Not determined, *BDL* Below detection level, – no value

^aPhase = mineral or glass phase analyzed; Emb = connected to interstitial glass channels glassy embayments in clinopyroxene and plagioclase, *CPX* host clinopyroxene, *PL* host plagioclase

xenoliths by Risku-Norja (1985), we believe that OL and CPX were equilibrated with the transporting magma over the entire *P–T* range and with interstitial glasses as well. This allows determination of pressure and temperature conditions of magma interaction with gabbroic rocks using the approach discussed by Danyushevsky et al. (1996). The announced uncertainties of the method are ±40°C and ±250 MPa at the 95% confidence level. A single-pyroxene geobarometer (Nimis 1995; ±200 MPa uncertainty at the 95% confidence level) was used to estimate depths of crystal mush formation. It is worth emphasizing that one great advantage of the Nimis (1995) geobarometer is that the calculation routine is based on the *P*-related element distribution between M1 and M2 suites in the CPX structure and,

thus, appears not to be very sensitive to relatively short event of pre-eruptive interaction of magma with gabbro xenoliths. This quality can be used to constrain pressure of crystal mush formation without introduction of an additional bias due to later CPX interaction with melt. Since gabbro xenoliths were more likely adiabatically transported to the surface, the average temperature of melt–gabbro interactions obtained using the Danyushevsky (2001) method (see subsequently) could also be used for pressure calculations with geobarometer of Nimis (1995).

Our calculations (Table 5 and Fig. 8) show that interstitial glasses and CPX-hosted glass embayments contain memory of only the last event of gabbro–melt interaction that occurred within a narrow interval of

Table 6 Trace element composition of host pillow-rim, interstitial and CPX- and PL-hosted glasses from gabbro nodules

Sample	K	Ti	V	Cr	Sr	Ba	Y	Zr	Nb	La	Ce	Pr	Nd	Sm
Host pillow-rim glass														
ICS01-8a	203	4,592	330	405	110	6.9	13.3	17.9	0.87	0.85	2.78	0.43	3.04	1.33
ICS01-8b	184	4,494	310	404	111	6.4	13.3	18.0	0.78	1.04	3.15	0.58	3.29	1.28
Glass crusts around gabbro nodules														
ICS01-8-8a	185	4,485	308	425	112	6.5	14.0	19.0	0.83	0.93	3.32	0.50	3.36	1.38
ICS01-8-8b	175	4,524	308	427	110	6.2	13.9	18.8	0.80	1.07	2.89	0.49	3.58	1.32
ICS01-8-13a-1	234	5,477	347	426	119	7.5	14.8	21.1	0.92	0.87	2.90	0.49	3.09	1.42
ICS01-8-13a-2	228	5,460	367	431	120	7.5	15.2	20.2	1.08	1.01	3.38	0.67	3.64	1.18
Interstitial glasses inside gabbro nodules														
ICS01-8-1a	247	5,256	380	468	125	8.1	15.4	20.4	1.09	1.11	3.32	0.57	3.41	1.34
ICS01-8-1d-1	201	4,787	376	391	106	6.5	13.9	18.3	0.79	1.00	2.90	0.55	3.17	1.15
ICS01-8-1d-2	196	4,739	367	400	107	5.5	14.6	18.5	0.93	0.72	2.93	0.51	3.10	1.10
ICS01-8-1e	218	5,071	357	463	112	6.9	14.2	19.2	1.00	1.08	2.90	0.58	3.42	1.19
ICS01-8-4a	251	4,777	336	448	114	8.2	15.3	21.0	0.90	0.96	3.45	0.59	3.49	1.22
ICS01-8-4b	256	5,068	350	481	119	8.6	15.7	22.3	1.26	1.04	3.46	0.71	3.64	1.42
ICS01-8-8c	255	4,251	306	463	110	8.1	13.2	19.2	1.05	1.13	3.32	0.50	3.17	1.04
ICS01-8-8d	250	4,095	297	467	108	7.5	12.6	18.5	0.93	1.13	3.02	0.59	3.03	0.96
ICS01-8-8f	230	4,046	270	459	109	7.6	13.1	18.4	1.07	1.11	3.42	0.66	3.04	1.09
ICS01-8-13a	359	5,480	367	429	117	7.6	15.4	21.3	1.09	1.12	3.46	0.65	3.58	1.65
ICS01-8-13b	358	4,690	318	432	119	11.5	14.1	23.1	1.66	1.38	3.76	0.73	3.65	1.57
ICS01-8-13c	229	5,268	355	420	119	9.7	15.2	23.4	1.30	1.33	3.90	0.76	4.13	1.58
ICS01-8-13d	338	5,024	341	482	121	11.6	15.8	26.2	1.86	1.52	4.20	0.64	4.12	1.67
Glassy embayments in CPX and PL														
ICS01-8-1														
181a-c1g1	263	5,403	397	468	132	8.5	15.7	20.4	0.91	1.17	3.47	0.64	4.02	1.04
181b-c2g1	246	5,520	390	482	131	8.7	15.1	20.6	1.20	1.11	2.90	0.52	3.81	1.24
181d-c4g1	185	4,768	367	424	99	6.4	14.0	17.4	0.80	0.96	2.76	0.54	3.40	1.21
181e-c5g2	234	5,178	375	486	117	7.2	14.3	19.8	1.00	0.93	3.15	0.61	3.39	1.26
ICS01-8-4														
184a-c1g1	278	4,612	312	389	113	8.4	15.2	19.5	0.96	1.08	3.07	0.59	3.35	1.27
184a-c1g2	249	5,010	356	448	117	8.1	16.2	21.7	1.05	1.17	3.53	0.67	3.42	1.24
184b-c1g1	244	4,913	347	444	115	8.0	15.2	20.5	1.11	1.14	3.45	0.68	3.50	1.25
184b-p1g1	275	5,243	357	491	123	8.8	16.2	23.6	1.19	1.34	3.72	0.64	3.90	1.42
184b-p1g2	411	5,175	366	485	132	12.4	16.2	23.6	1.34	1.30	3.87	0.72	3.68	1.56
184b-p1g3	270	5,195	349	493	122	9.3	16.6	24.0	1.19	1.31	3.61	0.71	3.82	1.55
ICS01-8-8														
188d-c4g1	243	4,027	301	465	107	7.2	12.4	17.5	0.94	0.96	3.00	0.49	3.09	1.11
188e-c5g1	210	4,407	302	531	110	7.8	14.0	21.5	1.07	1.16	3.41	0.55	3.56	1.49
ICS01-8-13														
1813a-c1g1	229	5,367	353	519	116	8.5	14.9	20.7	1.35	1.24	3.42	0.84	3.30	1.74
1813a-c1g2	255	5,419	373	500	119	8.8	15.3	24.3	1.24	1.26	3.74	0.67	3.75	1.64
1813b-c2g1	345	4,883	330	462	118	11.5	15.0	24.7	1.54	1.48	4.18	0.76	3.98	1.43
1813b-c3g1	283	5,207	353	487	118	9.7	15.1	24.9	1.50	1.36	4.01	0.66	4.10	1.46
1813c-c1g1	232	5,369	371	505	118	7.8	15.2	21.2	1.13	1.25	3.59	0.65	3.62	1.58
1813d-c4g1	338	5,024	341	482	120	11.9	15.5	26.4	1.58	1.69	4.24	0.80	3.97	1.59
1813a-p1m1	418	5,501	367	320	133	14.6	17.7	27.3	2.04	1.78	5.62	0.98	4.68	1.68
1813e-p1m1	359	5,480	364	429	126	13.0	16.8	27.7	1.94	1.77	4.58	0.81	4.49	1.67
1813e-p1m2	377	5,531	364	429	126	13.2	16.5	27.3	1.83	1.81	4.64	0.81	4.41	1.63
Sample	Eu	Gd	Dy	Ho	Er	Yb	[La/Sm] _n	[Ba/Nb] _n	[Sr/Sr*] _n	[Zr/Zr*] _n				
Host pillow-rim glass														
ICS01-8a	0.65	2.12	2.59	0.52	1.37	1.35	0.40	0.83	2.54	0.58				
ICS01-8b	0.56	2.57	2.74	0.57	1.59	1.48	0.51	0.86	2.32	0.57				
Glass crusts around gabbro nodules														
ICS01-8-8a	0.53	2.12	2.36	0.47	1.48	1.23	0.42	0.83	2.25	0.58				
ICS01-8-8b	0.58	1.99	2.54	0.52	1.47	1.49	0.51	0.81	2.30	0.57				
ICS01-8-13a-1	0.53	1.78	2.95	0.38	1.60	1.66	0.38	0.86	2.65	0.66				
ICS01-8-13a-2	0.62	2.29	2.72	0.55	1.65	1.62	0.54	0.73	2.30	0.64				
Interstitial glasses inside gabbro nodules														
ICS01-8-1a	0.63	2.63	3.09	0.49	1.58	1.65	0.52	0.78	2.49	0.62				
ICS01-8-1d-1	0.58	2.66	2.68	0.56	1.55	1.42	0.55	0.86	2.34	0.63				
ICS01-8-1d-2	0.50	2.28	2.71	0.53	1.52	1.36	0.41	0.62	2.37	0.65				
ICS01-8-1e	0.60	2.14	2.71	0.46	1.40	1.61	0.57	0.72	2.39	0.62				
ICS01-8-4a	0.60	2.25	2.68	0.60	1.77	1.84	0.49	0.96	2.20	0.67				
ICS01-8-4b	0.67	2.69	2.81	0.54	1.67	1.90	0.46	0.72	2.24	0.64				

Table 6 (Contd.)

Sample	Eu	Gd	Dy	Ho	Er	Yb	[La/Sm] _n	[Ba/Nb] _n	[Sr/Sr*] _n	[Zr/Zr*] _n
ICS01-8-8c	0.48	2.05	2.20	0.44	1.18	1.17	0.68	0.81	2.28	0.69
ICS01-8-8d	0.52	1.49	2.14	0.44	1.27	1.25	0.74	0.85	2.38	0.71
ICS01-8-8f	0.52	1.97	2.27	0.46	1.31	1.37	0.64	0.74	2.26	0.66
ICS01-8-13a	0.67	2.51	2.65	0.50	1.83	1.62	0.42	0.73	2.23	0.57
ICS01-8-13b	0.62	2.26	2.55	0.41	1.51	1.63	0.55	0.73	2.15	0.63
ICS01-8-13c	0.73	2.38	2.74	0.55	1.57	1.66	0.53	0.78	1.99	0.60
ICS01-8-13d	0.62	1.62	2.69	0.53	1.68	1.82	0.57	0.66	1.95	0.65
Glassy embayments in CPX and PL										
ICS01-8-1										
181a-c1g1	0.64	2.11	2.79	0.63	1.71	1.67	0.99	0.70	2.38	0.65
181b-c2g1	0.67	2.51	2.51	0.51	1.47	1.71	0.76	0.56	2.63	0.62
181d-c4g1	0.63	1.98	2.72	0.59	1.68	1.33	0.84	0.50	2.17	0.56
181e-c5g2	0.57	2.38	2.69	0.53	1.64	1.47	0.76	0.46	2.39	0.63
ICS01-8-4										
184a-c1g1	0.64	2.10	2.45	0.54	1.44	1.48	0.93	0.53	2.36	0.62
184a-c1g2	0.69	2.68	2.80	0.62	1.71	2.13	0.81	0.59	2.25	0.69
184b-c1g1	0.66	2.59	2.83	0.50	1.61	2.09	0.75	0.57	2.21	0.64
184b-p1g1	0.67	2.78	2.72	0.58	1.59	1.87	0.78	0.59	2.17	0.66
184b-p1g2	0.65	2.41	3.18	0.56	1.83	2.01	0.97	0.52	2.34	0.64
184b-p1g3	0.73	2.05	3.06	0.57	1.71	2.13	0.82	0.53	2.19	0.65
ICS01-8-8										
188d-c4g1	0.48	2.02	2.19	0.42	1.33	1.27	0.81	0.54	2.35	0.62
188e-c5g1	0.63	2.37	2.62	0.58	1.50	1.52	0.77	0.49	2.12	0.61
ICS01-8-13										
1813a-c1g1	0.76	2.17	3.64	0.53	1.63	1.40	0.66	0.45	2.32	0.56
1813a-c1g2	0.54	2.66	2.67	0.55	1.79	1.65	0.75	0.48	2.13	0.64
1813b-c2g1	0.63	2.35	2.62	0.53	1.77	1.64	0.78	0.65	1.94	0.68
1813b-c3g1	0.55	2.98	2.78	0.53	1.74	1.80	0.68	0.59	1.95	0.67
1813c-c1g1	0.55	2.60	2.78	0.57	1.57	1.66	0.72	0.49	2.20	0.58
1813d-c4g1	0.69	2.10	2.76	0.53	1.57	1.81	0.79	0.67	1.96	0.69
1813a-p1m1	0.79	2.35	2.98	0.65	1.85	2.02	0.75	0.66	1.73	0.64
1813e-p1m1	0.66	2.73	2.92	0.58	1.76	1.97	0.70	0.66	1.86	0.66
1813e-p1m2	0.63	2.75	2.88	0.60	1.76	1.89	0.76	0.69	1.86	0.67

Trace element concentrations are given in ppm; for further detail, see explanation notes for Table 1

temperatures ($1,210 \pm 15^\circ\text{C}$; Fig. 8a) and very low pressures (40 ± 120 MPa; Fig. 8b) corresponding in fact to the P - T conditions of magma quenching (i.e., $1,190$ – $1,220^\circ\text{C}$ and 60 ± 100 MPa obtained from outer glassy rims and host pillow rim glasses; all average values here and hereafter are given at $\pm 2\sigma$ standard deviation). These systematically higher than atmospheric pressures should be considered as reflecting those of magma quenching since the entire variations are well inside the uncertainty of calculations. Alternatively, this shift to somewhat higher values could be interpreted also as that resulted from sub-glacial character of eruptions at Midfell. This is, however, impossible to justify qualitatively at the ± 250 MPa uncertainty of calculations.

Low S concentrations in interstitial glasses and glassy embayments suggest pronounced pre-eruptive magma degassing. In contrast, the single-pyroxene geobarometer of Nimis (1995) provides systematically higher pressures (total range from 110 to 800 MPa, average = 340 ± 160 MPa calculated for the average temperature of $1,210^\circ\text{C}$) that obviously reflects the depths of magma reservoir location. This estimate corresponds to the geophysical data of Björnsson (1985) and to the results of fluid inclusion study by Hansteen (1991).

Discussion

Partial melting of gabbro

Overall reversal zoning of nodule-forming minerals, strongly resorbed, porous texture of clinopyroxene, high-volume fraction of the interstitial glass suggest that partial melting of gabbro cumulates might be very probable. In order to constrain trace element composition of the resulting melt, we examined modal batch melting (Shaw 1970). We restricted our choice to this mechanism because gabbro nodules contain very high proportion of melt relative to solid (9–22%; Table 1) that makes batch melting more favorable compared to other melting models. We employed a set of mineral–melt partition coefficients based on the compilations by Gurenko and Chaussidon (1995), Halliday et al. (1995), White (1997) (Table 7). As a bulk solid, we used averaged composition of the Midfell gabbro nodules from which we subtracted the glass fraction (Table 7). Since interstitial glass and host gabbro nodules exhibit sub-parallel trace element patterns, such glass subtraction does not significantly change the existing element-to-element ratios and is just a nearly parallel shift of mostly

all element concentrations towards lower values. The amount of mineral phases in the bulk solid were accounted by mass-balance calculations using individual bulk-rock compositions of gabbro nodules and compositions of their rock-forming minerals. They appeared to be very similar to those obtained on the basis of computer analysis of the digital images (Table 2). We, however, prefer using the mass-balance calculated values since the uncertainty of the computer analyses appears to be very high. In addition, some minor phases, as for instance olivine, remain unidentified by computer analyses. Olivine is present in trace (<1%) amount in the gabbro xenoliths (petrographic observation) and 0.2–2.2% were obtained from mass-balance calculations (Table 2). However, olivine was never identified by computer analyses. Furthermore, slide images allow only a two-dimensional analysis of phase distribution and therefore can result in incorrect estimation of volume proportions of mineral phases.

The compositions of melts resulted from 1 to 40% of partial melting (Table 7) are shown in Fig. 9. Melts

corresponding to 10–20% melting degree are characterized by pronounced Sr excess ($[\text{Sr}/\text{Sr}^*]_n = 1.3\text{--}2.1$), satisfactorily reproducing the compositions of natural glasses in most trace elements but not in Ba concentrations which appear to be too high. The $[\text{Ba}/\text{Nb}]_n$ ratios range from 1.9 to 2.6 in the calculated partial melts, whereas the glasses associated with gabbro nodules show $[\text{Ba}/\text{Nb}]_n$ ratios of 0.5–1.0 (Table 6). Only the melt produced by 1% of partial melting has $[\text{Ba}/\text{Nb}]_n$ ratio of 0.7. However, the $[\text{Sr}/\text{Sr}^*]_n$ ratio of this melt is also 0.7 (Table 7) that does not match the compositions of natural glasses at all. This is, in fact, the strongest constraint that completely rules out the model of gabbro partial melting. High $[\text{Ba}/\text{Nb}]_n$ ratios in the partial melts follow straight forward from the extremely high $[\text{Ba}/\text{Nb}]_n$ ratio of the source gabbro. The resulting liquid phase will be always relatively more enriched in Ba than in Nb yielding $[\text{Ba}/\text{Nb}]_n > 1$ (Fig. 9). We suggest, therefore, that the gabbro partial melting is not the process leading to the observed geochemical signatures of the nodule-related glasses.

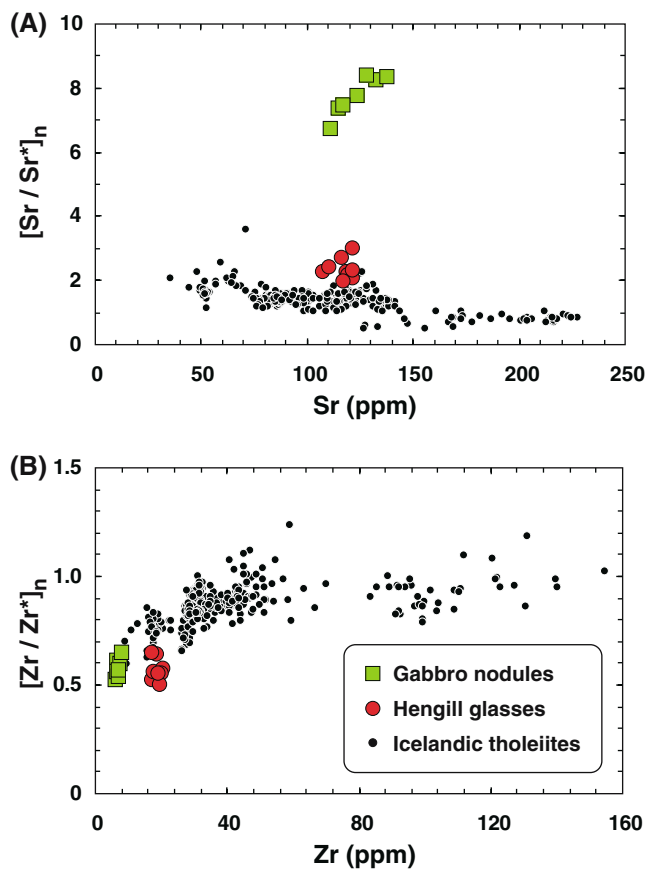


Fig. 7 Strontium positive (a) and Zr negative (b) anomalies in the Midfell glasses and associated gabbro nodules. Data source for Icelandic tholeiites are similar as pointed in Fig. 5. In this figure and Fig. 12, $[\text{Sr}/\text{Sr}^*]_n$ and $[\text{Zr}/\text{Zr}^*]_n$ ratios represent magnitudes of Sr and Zr anomalies normalized to chondrite and defined as $[\text{Sr}]_n/([\text{Ce}]_n \times [\text{Nd}]_n)^{0.5}$ and $[\text{Zr}]_n/([\text{Nd}]_n \times [\text{Sm}]_n)^{0.5}$, respectively. Note that Midfell glasses are characterized by the most pronounced Sr excess among a large number of Icelandic tholeiites in general

Mixing of gabbro partial melts with “uncontaminated” magma

Another scenario that should be examined to explain trace element signatures of the glasses associated with gabbro nodules is mixing of melts resulted from gabbro partial melting (Table 7) with presumably “uncontaminated” Icelandic tholeiitic magma—the magma whose chemical composition was not affected by interaction with the Icelandic crustal rocks. To define potentially “uncontaminated” magma composition that is relevant for Icelandic rift-related tholeiites is not a simple question, taking into account the entire compositional spectrum of glasses (shaded field in Fig. 6) and the fact that crust-magma interaction could be widespread in Iceland. We suggest the following conditions:

1. The magma should be erupted and present within the neovolcanic rift zone of Iceland and be timely and spatially related to the Midfell volcanism.
2. It should not demonstrate remarkable enrichment in Sr chondrite-normalized concentrations and have $[\text{Ba}/\text{Nb}]_n$ ratio < 1.
3. It is very well known that Midfell rift-related tholeiites are characterized by somewhat elevated CaO contents and lower Al_2O_3 , as compared to MORB, and these signatures were ascribed to different mechanisms of magma interaction with the Icelandic crustal rocks (Fig. 6 in Trønnes 1990). Although there is an uncertainty in quantitative definition of the absolute CaO and Al_2O_3 contents in the Icelandic “uncontaminated” magma, we believe that CaO/ Al_2O_3 ratio of this magma has to be lower than that of the Midfell lavas which are too rich in CaO to be in equilibrium with a lherzolite source at high pressures in accordance with the criteria of Kinzler and Grove (1992a, b).

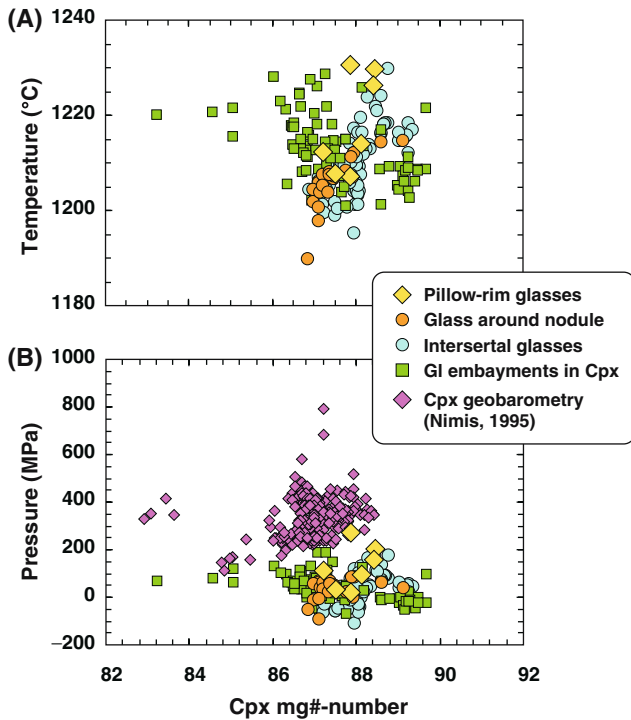


Fig. 8 Temperature (a) and pressure (b) conditions versus *mg*-number of clinopyroxene from gabbro nodules. Temperature and pressure of melt–nodule interaction are calculated following the approach of Danyushevsky et al. (1996) (see text for details). Artificial negative pressures are due to the existing uncertainty of pressure calculations (i.e., ± 250 MPa). The *mg*-numbers are used to outline the positions of outer glassy rinds and host pillow rim glasses are calculated *mg*-numbers of clinopyroxene to be in equilibrium with the glasses

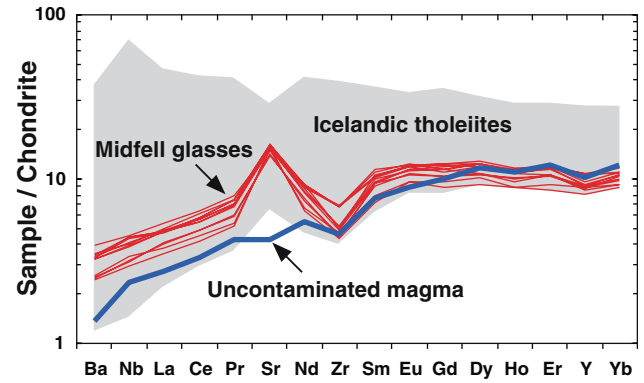


Fig. 10 Chondrite-normalized trace element composition of pre-sumably “uncontaminated” magma used for calculation of binary mixing with melts resulted from partial melting of gabbro (Fig. 11) and for modeling of melt percolation through gabbroic matrix (Fig. 12). The compositions of Icelandic tholeiites (data sources are similar as pointed in Fig. 5) are given for comparison; *Midfell glasses* are nodule-bearing host pillow-rim glasses, as given in Fig. 5. Chondrite normalizing values are taken from Anders and Grevesse (1989)

Following to these criteria, the composition of such “uncontaminated” magma (Table 8) was selected to be similar to those of the tholeiitic basalts erupted within the neovolcanic rift zone of Iceland and is based on the compositions of the Reykjanes quenched glasses (author’s unpublished data). The $\text{CaO}/\text{Al}_2\text{O}_3$ ratio of 0.75 results from 16 wt% Al_2O_3 and 12 wt% CaO and is based on the experimental data from spinel peridotite melting and basaltic magma crystallization summarized

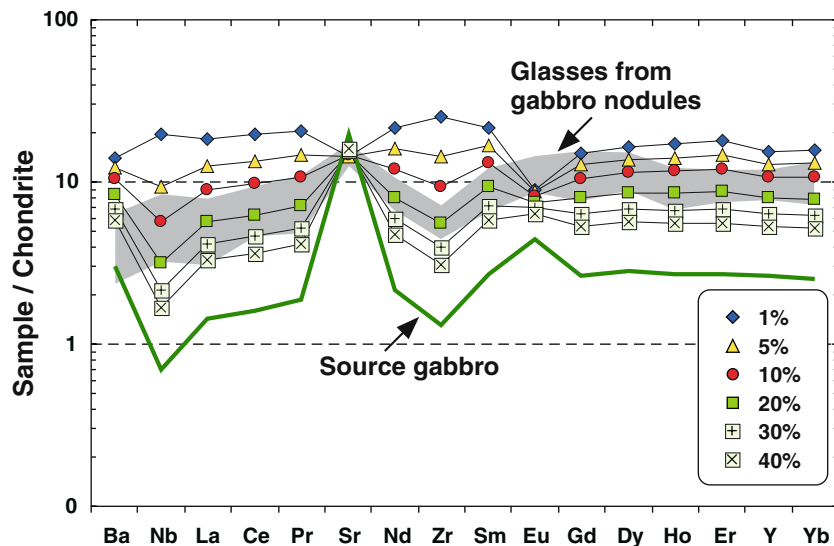


Fig. 9 Calculated trace element concentrations of melts resulted from partial melting of gabbro. Melt compositions were calculated using modal batch melting (Shaw 1970) of a source compositionally similar to the Midfell gabbro nodules (see text for detail). Distribution coefficients used represent a compilation of those given in Gurenko and Chaussidon (1995), Halliday et al. (1995)

and White (1997). *Source gabbro* composition of the solid used in modeling. *Shaded field* represents compositions of interstitial glasses and CPX- and PL-hosted glassy embayments from the studied gabbro nodules. Melts resulted from 10–20% partial melting match the compositions of natural glasses, except for $[\text{Ba}/\text{Nb}]_n$ ratios

Table 7 Modeling of gabbro partial melting

Element	OL	CPX	PL	SP	D_{bulk}	Gabbro bulk solid ^b
Partition coefficients ^a						
Ti	0.015	0.384	0.0468	0.15	0.1600	1,451
Sr	6.3E-05	0.1283	2.1	0	1.3758	153
Y	0.0082	0.467	0.013	0.004	0.1626	4.1
Zr	6.8E-04	0.1234	0.001	0.06	0.0427	5.2
Nb	5.0E-05	0.0077	0.033	0.08	0.0253	0.17
Ba	3.4E-06	6.8E-04	0.33	0	0.2098	7.2
La	3.1E-05	0.0858	0.082	0.0006	0.0804	0.34
Ce	1.9E-05	0.072	0.072	0.0006	0.0695	0.98
Pr	4.9E-05	0.15	0.056	0.0006	0.0851	0.17
Nd	4.2E-04	0.1873	0.045	0.0006	0.0904	0.98
Sm	4.5E-04	0.291	0.033	0.0006	0.1170	0.40
Eu	7.5E-04	0.43	0.55	0.0006	0.4912	0.25
Gd	0.0011	0.44	0.034	0	0.1668	0.52
Dy	0.0027	0.442	0.03	0.0015	0.1650	0.69
Ho	0.0093	0.4	0.0245	0.0015	0.1477	0.15
Er	0.0109	0.387	0.02	0.003	0.1406	0.43
Yb	0.024	0.43	0.014	0.0045	0.1512	0.41
Mineral proportions ^b						
Gabbro	0.012	0.330	0.635	0.023	—	—
F (%) ^c	1	5	10	20	30	40
Compositions of partial melts ^d						
Ti	8,615	7,182	5,946	4,423	3,522	2,925
Sr	112	113	114	118	121	125
Y	24.0	20.1	16.6	12.4	9.9	8.2
Zr	99.4	57.4	37.6	22.2	15.8	12.2
Nb	4.8	2.3	1.4	0.8	0.5	0.4
Ba	33.1	28.9	24.9	19.6	16.1	13.7
La	3.8	2.7	2.0	1.3	1.0	0.8
Ce	12.4	8.4	6.0	3.8	2.8	2.2
Pr	1.8	1.3	1.0	0.6	0.5	0.4
Nd	9.8	7.2	5.4	3.6	2.7	2.2
Sm	3.2	2.5	1.9	1.4	1.0	0.9
Eu	0.5	0.5	0.5	0.4	0.4	0.4
Gd	3.0	2.5	2.1	1.6	1.2	1.0
Dy	4.0	3.3	2.8	2.1	1.7	1.4
Ho	1.0	0.8	0.6	0.5	0.4	0.3
Er	2.9	2.3	1.9	1.4	1.1	0.9
Yb	2.6	2.1	1.7	1.3	1.0	0.8
[La/Sm] _n	0.74	0.68	0.66	0.58	0.63	0.56
[Ba/Nb] _n	0.72	1.32	1.87	2.58	3.39	3.60
[Sr/Sr*] _n	0.68	0.97	1.34	2.14	2.95	3.81
[Zr/Zr*] _n	1.16	0.89	0.77	0.65	0.63	0.57

^aMineral–melt partition coefficients for OL, CPX, PL and SP are taken from the compilations by Gurenko and Chaussidon (1995), Halliday et al. (1995), White (1997)

^bChemical composition and mineral proportions of the bulk solid gabbro used in modeling. It represents an average bulk-rock composition of seven studied gabbro nodules (given in Table 2), from which the proportion of interstitial glass is subtracted. The proportions of mineral and glass phases composing the nodules were calculated using mass–balance method

^cF degree of partial melting

^dCompositions of partial melts calculated from modeling of modal batch melting (Shaw 1970)

by Kinzler and Grove (1992a). We, therefore, believe that this magma represents more probably a melt which (1) would have originated by partial melting of a lherzolite mantle source at $P = 1.0\text{--}1.5$ GPa (see Fig. 8 in Gurenko and Chaussidon 1995) and then, (2) would have been subjected to substantial low-pressure OL fractionation. We emphasize that such melt is in equilibrium with olivine but undersaturated with plagioclase and clinopyroxene at relatively low-crystallization pressures (i.e., 350 MPa—a lithostatic pressure resembling that of xenolith's origin), as follows from the calculated

pseudo-liquidus temperatures of these phases ($T_{\text{ol}} = 1,252^\circ\text{C}$ calculated using the model of Ford et al. 1983; $T_{\text{pl}} = 1,226^\circ\text{C}$ —average calculated from the models of Ariskin and Barmina (1990), Weaver and Langmuir (1990) and Ariskin et al. (1993); $T_{\text{cpx}} = 1,222^\circ\text{C}$ —average calculated from the models of Ariskin et al. (1987), Weaver and Langmuir (1990) and Ariskin et al. (1993); calculations were done at oxygen fugacity conditions corresponding to FMQ buffer). Further differentiation of such melt at 350 MPa will result in crystallization of OL, then OL + PL and finally OL + PL + CPX

mineral assemblages. The concentrations of trace elements are those as found in the most primitive Reykjanes glasses (author's unpublished data), while Sr concentration is an extrapolated value calculated as $Sr^* = (Ce \times Nd)^{0.5}$ to avoid the common for Icelandic tholeiites Sr-enrichment (Fig. 10, Table 8).

Mixing relations between melts resulted from 1 to 40% of gabbro partial melting (Table 7; Fig. 9) with earlier discussed "uncontaminated" Icelandic tholeiitic magma composition are shown in Fig. 11. It is essential that the $[Ba/Nb]_n$ and $[Sr/Sr^*]_n$ variations observed in the nodule-related glasses could be accounted by mixing with neither selected "uncontaminated" magma composition nor any other composition of magma because it requires admixture of different types of gabbro partial melts i.e., those resulted from 1 to 5% melting to account for low $[Ba/Nb]_n$ ratios (Fig. 11a) and those resulted from 10 to 40% melting to account for high $[Sr/Sr^*]_n$ ratios (Fig. 11b), in both cases suggesting unrealistically high fraction of the proposed contaminant.

Melt infiltration through gabbro crystal mush

Melt percolation and coupled chromatographic effects can efficiently affect composition of the migrating liquid (e.g., Navon and Stolper 1987; Bodinier et al. 1990; Batanova et al. 1998; Boudreau and Meurer 1999). Here, we discuss a case where a tholeiitic magma migrates through porous, gabbroic rocks and demonstrate that this process can substantially modify the original major and trace element concentrations in the migrating melt, giving an explanation for the compositional discrepancy observed in the Midfell gabbro xenoliths and associated with them glasses. We use a computer program IRIDIUM that explores mineral-liquid equilibrium with one-dimensional, compaction-driven mass transport equations to model a phenomenon of melt infiltration and its reaction with wall-rocks (Boudreau 2003). The program calculates mineral precipitation/dissolution and simulates chromatographic fronts of elements caused by percolation of a silicate liquid through a porous solid media. The mineral-melt equi-

Table 8 Modeling of melt percolation through gabbro rocks

Sample	Reyk-Gl ^a	4 m	8 m	12 m	16 m
Note	Uncont/inf	Resulting liquid ^b			
SiO ₂	50.0	50.1	49.0	49.1	48.8
Al ₂ O ₃	16.0	14.0	14.3	14.5	14.7
FeO	9.0	8.9	8.8	8.1	7.5
MgO	10.0	10.1	10.8	10.9	11.3
CaO	12.0	14.5	15.4	15.6	16.0
Ti	5,990	6,232	6,248	5,821	4,664
Sr	33	70	105	105	106
Y	15.9	16.7	16.8	16.1	13.5
Zr	18.1	18.3	18.4	18.4	18.7
Nb	0.57	0.6	0.6	0.6	0.6
Ba	3.2	3.1	4.3	12.6	16.2
La	0.64	0.6	0.6	0.7	0.9
Ce	1.99	2.0	2.0	2.1	2.7
Nd	2.49	2.5	2.5	2.6	3.0
Sm	1.12	1.2	1.2	1.2	1.2
Eu	0.50	0.5	0.4	0.4	0.4
Gd	1.95	2.0	2.1	2.0	1.7
Dy	2.81	3.0	3.0	2.8	2.2
Ho	0.62	0.6	0.7	0.6	0.5
Er	1.92	2.0	2.0	1.9	1.5
Yb	1.99	2.1	2.1	2.0	1.5
CaO/Al ₂ O ₃	0.75	1.04	1.08	1.08	1.09
$[La/Sm]_n$	0.36	0.31	0.31	0.37	0.47
$[Ba/Nb]_n$	0.59	0.54	0.75	2.21	2.84
$[Sr/Sr^*]_n$	0.99	2.10	3.14	3.01	2.49
$[Zr/Zr^*]_n$	0.71	0.69	0.70	0.68	0.65

Modeling of melt percolation through gabbroic solid rocks was performed using the program IRIDIUM 5.10Beta (Boudreau 2003) (see text for detail)

^aTrace elements are similar as given in Table 7. Composition of "uncontaminated" magma used for calculation of mixing relations with gabbro partial melts (Fig. 11) and taken as a composition of melt infiltrating through the gabbroic matrix (Fig. 12). It was selected to resemble those of the tholeiitic basalts erupted within the neovolcanic rift zone of Iceland and containing 1.75 wt% Na₂O, 0.02 wt% K₂O and 0.03 wt% P₂O₅; CaO and Al₂O₃ contents were selected to match those of MORB (Trønnes 1990 and references therein) giving CaO/Al₂O₃ ratio of 0.75. The concentrations of trace elements are the lowest among those found in Reykjanes tholeiitic glasses (author's unpublished data), while Sr concentration represent extrapolated value calculated as $(Ce \times Nd)^{1/2}$ to avoid common for Icelandic tholeiites enrichment in Sr relative to other trace elements

^bComposition of infiltrating melts "extracted" from gabbroic column at the 4th, 8th, 12th, and 16th m and whose locations are shown in Fig. 12

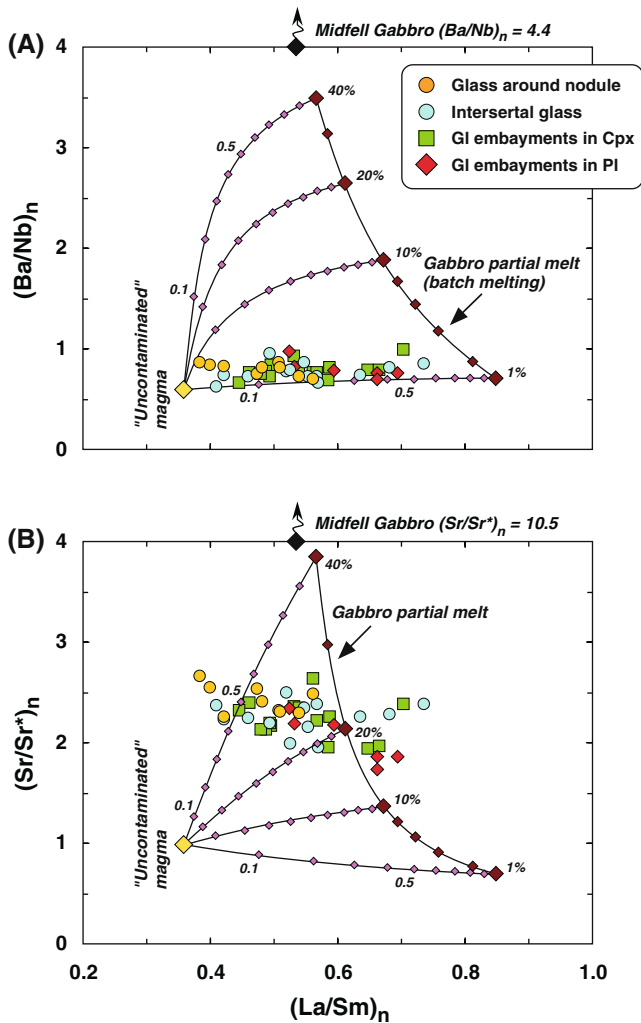


Fig. 11 Mixing of presumably “uncontaminated” magma with melts produced by partial melting of gabbro. Trace element composition of the “uncontaminated” magma is outlined in Fig. 10 and discussed in the text; the *gabbro partial melt solid line* represents melt composition originated due to 1–40% batch partial melting of gabbroic rocks (see text and Fig. 9). We emphasize that such mixing scenario cannot account for the composition of glasses associated with gabbro nodules because it requires admixture of different types of partial melts i.e., 1–4% melts to achieve $[\text{Ba}/\text{Nb}]_n$ ratios (a) and 20 to 40% melts for $[\text{Sr}/\text{Sr}^*]_n$ ratios (b) suggesting in both cases unrealistically high fraction of the contaminant. The $[\text{Sr}/\text{Sr}^*]_n$ ratios are calculated similarly as this outlined in Fig. 7

librium part of the IRIDIUM program is based on a free energy minimization algorithm as used in MELTS software (Ghiorso and Sack 1995). Furthermore, IRIDIUM incorporates both general and compaction-driven thermal and mass transport equations derived by McKenzie (1984) (for more detail, see Boudreau 2003). Modeling is started with calculation of initial equilibrium state of the system. This includes calculation of the equilibrium mineral assemblages through the entire column length based on the input bulk solid composition, temperature and pressure, and the composition of liquid equilibrated with the bulk solid at given P – T conditions. The program continuously recalculates

current mineral, major and trace element compositions of the remaining bulk solid, as well as the compositions of the resulting melt and coexisting fluid performing such calculations for each node over the entire column length.

We modeled infiltration of a tholeiitic magma through solid rocks which are compositionally similar to the Midfell gabbro xenoliths. Similarly as in the case of partial melting, we used averaged composition of solid residue remained after mass-balance subtraction of the melt fraction from the compositions of gabbro nodules; Table 7). The composition of infiltrating melt was that of the “uncontaminated” magma discussed earlier (Fig. 10, Table 8). The temperature of 1,250°C (calculated liquidus temperature of the infiltrating melt by IRIDIUM) and pressure of 350 MPa were taken to be constant over the entire length of an arbitrary selected 20 m long chromatographic column. The flux rate of the incoming melt was varied between 1 and 10 cm/day that appeared to be reasonable for such processes (A. Boudreau, personal communication, 2004). The parameters selected represent a rather simple case of melt infiltration since our task here is, using the simplest example, to demonstrate more clearly the effects of melt percolation on the composition of the migrating melt. We emphasize, however, that the difference in some important input parameters, such as column length, temperature, pressure or flux rate, results in only variations in temporal scale and has no effect on the relative migration rates of the elements characterized by different incompatibility because a speed of migration of an element directly relates to its bulk solid–melt distribution coefficient (Navon and Stolper 1987).

The results of our calculations are given in Table 8 and presented in Figs. 12, 13. Our percolation model has satisfactorily explained the composition of whole rock lavas erupted in the Midfell area, as well as for melts to be present in gabbro xenoliths as interstitial glasses and glass embayments (Fig. 13). In more detail, the melt percolation model reproduces in detail the observed relatively high $[\text{Sr}/\text{Sr}^*]_n$ ratios coexisting with low (i.e., < 1) $[\text{Ba}/\text{Nb}]_n$ ratios. This occurs because Ba is more incompatible than Sr in the chromatographic process (bulk $D_{\text{Ba}} = 0.21$ vs. bulk $D_{\text{Sr}} = 1.38$ in Table 7) causing faster percolation and saturation of the chromatographic column in Ba compared to Sr (Fig. 12d, e). On the other hand, we emphasize that we did not tend to exactly reproduce the compositions of the erupted in Midfell lavas but to suggest a viable mechanism explaining low Ba/Nb ratios in the melts coexisting with gabbro having very high Ba/Nb ratios.

As follows from the model calculations, the reaction of infiltrating melt with gabbro solid results in a crystal mush composed of ~80% PL, ~15% OL and ~5% melt fraction located in the bottom few meters of the column. This indicates that the reaction involves crystallization of plagioclase and olivine combined with the resorption of clinopyroxene; the latter occurs due to stronger undersaturation of the infiltrating melt in CPX than in OL

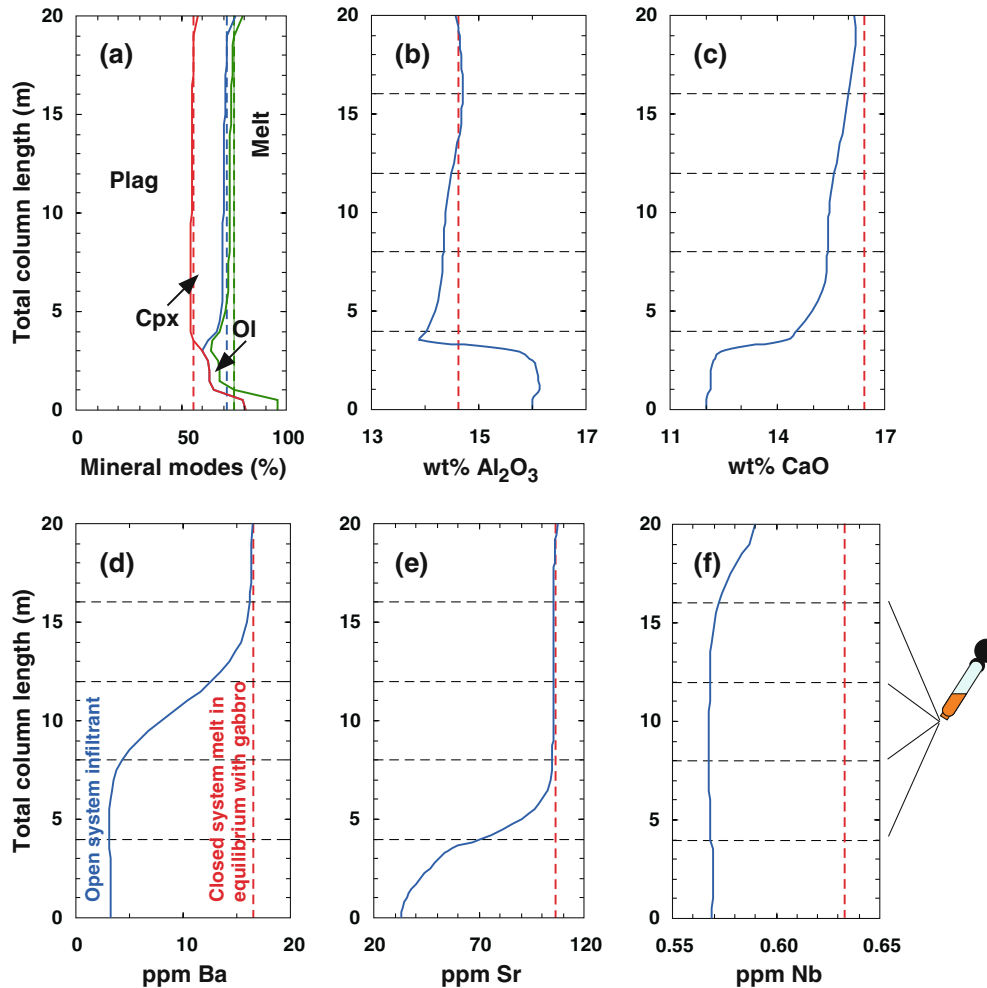


Fig. 12 Calculated chromatographic effects on chemical composition of melts percolating through gabbroic matrix (see text for detail). **a** Calculated mineral composition of the crystal mush column. *Vertical, dashed lines* represent initial proportions of mineral and melt phases (i.e., *Ol* olivine, *Cpx* clinopyroxene, *Plag* plagioclase, and *Melt*); *solid lines* proportions of the composing solid and melt phases resulted from the 56-day long percolation of infiltrant. **b–f** Distribution of Al_2O_3 (**b**), CaO (**c**), Ba (**d**), Sr (**e**) and Nb (**f**) concentrations over the length of the chromatographic column (selected total length of 20 m). *Vertical, dashed lines* return the composition of initial melt in equilibrium with gabbro mush prior the infiltration began, i.e., closed system melt in equilibrium with gabbro in panel (**d**); *solid line* composition of hybrid melt i.e.,

open system infiltrant in panel (**d**). *Tiny, horizontal, dashed lines* in (**b–f**) panels return positions of infiltrant in the chromatographic column at 56th day of melt percolation and whose trace element compositions are shown in Fig. 11 and Table 8. The calculation was performed using the program IRIDIUM 5.10 Beta version (Boudreau 2003). We emphasize that this figure outlines a “frozen” state of the chromatographic column at 56th day of melt percolation and cannot be used to evaluate relative proportions of compositionally different types of magmas either erupted on the surface or remained staying in the magmatic mush column; this figure illustrates a relative migration rates of elements of different incompatibility

and PL. Systematic overgrowth of PL crystals composing the nodules by more calcic PL (Fig. 3a), as well as the presence of pure plagioclase-bearing types of xenoliths in the Midfell lavas (Risku-Norja 1985) and gabbro–anorthosite nodules from the Krisuvik fissure swarm, Reykjanes Peninsula, Iceland (Høj 1993) independently support the conclusion that the reaction outlined in Fig. 12 may be quite common within the Icelandic crust. We also emphasize that similar mechanism of melt percolation may be regarded as an alternative explanation for the elevated $\text{CaO}/\text{Al}_2\text{O}_3$ ratios observed in primitive Hengill and Reykjanes tholeiitic

glasses that were first addressed by Trønnes (1990), who proposed fractionation of olivine and plagioclase combined with 5–30% assimilation of clinopyroxene.

Insights into the magma chamber processes

Geophysical evidence indicates that the Icelandic crust has an average thickness of 15–25 km under the Tertiary lava plateaus decreasing to about 10 km under the rift zones (Björnsson 1985). The metamorphic zonation of the Icelandic crust is generally similar to oceanic crust,

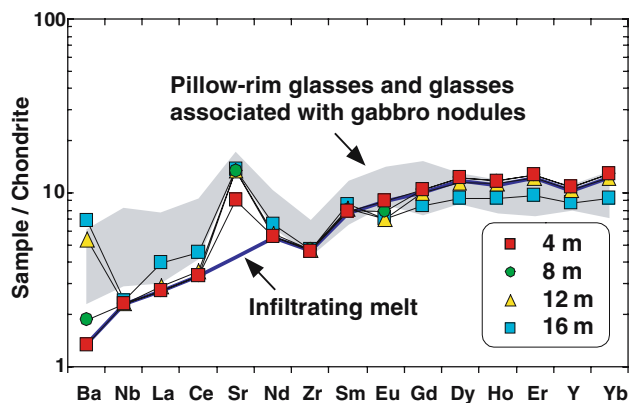


Fig. 13 Chondrite-normalized multi-element diagram of percolating melts given in comparison with nodule-bearing pillow-rim glasses, interstitial glasses, CPX- and PL-hosted glassy embayments (shaded field)

as inferred from geophysical measurements, data from geothermal wells, as well as from the geological structure of the denudated Tertiary formation. Four layers accordingly to the grades of metamorphism i.e., zeolite (Layer 1, 0–4 km), chlorite–epidote to greenschist (Layer 2; 4–6 km), low- to high-grade amphibolite (Layer 3; 4–12 km), and granulite facies (Layer 4, below 8–12 km) were recognized (Óskarsson et al. 1982). The transition from low- to high-grade amphibolite facies is accompanied by crustal anatexis that starts near the 650°C isotherm at about 5 km depth (Óskarsson et al. 1982), while the upper part of Layer 3 consists of water saturated rocks with a porosity of 1–3% (Björnsson 1977). The temperature regime of the Icelandic crust (Pálmason 1971, 1973, 1980; Hermance and Grillo 1974) is consistent with the assumption of a partially molten layer to be probably present in a form of cumulate-forming magma chambers, intrusive bodies and dikes at the top of Layer 4. The presence of a low resistance, partially molten layer extending under most Iceland was supported by magnetotelluric measurements at about 70 sites (e.g., Beblo and Björnsson 1978, 1980; Thayer et al. 1981; Beblo et al. 1983).

This comprehensively constrained structure of the Icelandic crust gives an important basis for the reconstruction of magma chamber processes at the Hengill area. The Midfell gabbro nodules studied represent products of PL + CPX ± OL ± SP crystallization. It is unlikely that they are crystallization products of the transporting magma. However, as reported by Risku-Norja (1985) and shown in the present study, the nodules might have originated from a geochemically very similar type of earlier crystallized magmas. The pressure range spreads from 350 ± 100 to 40 ± 60 MPa (Fig. 10b) and is in a good agreement with experimental data and calculation results reported by Risku-Norja (1985) and Hansteen (1991). We believe that the high-pressure edge limit of 350 MPa reflects the conditions, at which the gabbroic crystal mush might have been formed. The lower pressures ranging from ca. 200 MPa down to

near-atmospheric values reflect more likely the shallow-depths to near-surface conditions, at which the transporting magma continued to react with its hosted gabbroic fragments. The estimated residence time of gabbro xenoliths in the magma could be bracketed between 1 day and 1 month, as inferred from Fe–Mg zoning of the cognate OL phenocrysts (Gurenko et al. 2004). We propose the following sequence of events that likely occurred in the Hengill magmatic system and explaining the origin of gabbro xenoliths.

Stage 1 Creation of a gabbroic crystal mush. The origin of PL + CPX ± OL ± SP gabbro cumulates is ascribed to earlier crystallization of melts which are compositionally similar to the transporting magmas; their crystallization occurred in magma reservoirs located at about 10 km depth corresponding to the crust-mantle boundary beneath the neovolcanic rift zone of Iceland (e.g., Björnsson 1985). We do not see any geochemical signature of this stage in the compositions of nodule-forming minerals and believe that it was completely erased by subsequent percolation of melts and thus could not be reconstructed in detail here.

Stage 2 Repeated selective re-crystallization of CPX followed by its partial dissolution and, in lesser extent, of PL, both deposited in the cumulative crystal mush layer, due to reaction with migrating melts in accordance with melt percolation model discussed before. Such melt–rock interactions accompanied by mutual melting–crystallization events result in decrease of CPX nucleation centers, thereby causing formation of large CPX oikocrysts composing gabbro nodules in a scale from a few to a few tens cm. Formation of a network (interstitial glasses and glass embayments in CPX) filled by melts relatively enriched in CaO and Sr, and characterizing by varying Ba/Nb ratios is ascribed to this stage. The residual signature of nodule-forming plagioclase follows from its subidiomorphic, randomly oriented crystals which look to be more resistant to melt–rock interactions than the neighboring clinopyroxene. Clinopyroxene has preferentially xenomorphic grain shapes and looks to be more actively reacting with the interstitial melt.

Stage 3 Fragmentation of a brittle gabbro layer followed by nearly adiabatic transport of the rock fragments to the surface. We suggest fragmentation of earlier solidified CPX–PL crystal mush preferentially along cleavage planes in the large CPX oikocrysts resulting in gabbro fragments whose size is limited to that of the CPX monocrystal fragments. We consider that as a very possible reason to explain simultaneous CPX extinction over the entire thin section square observed in the series of slides cutting in different directions of individual gabbro nodules. Compositional overlap between host pillow rim glasses, interstitial glasses inside gabbro nodules, glass embayments in CPX coupled with reverse

zoning of composing minerals suggest that gabbro xenoliths were not subjected to substantial partial melting in the transporting magma. However, the remarkable pressure release from ca. 350 MPa to atmospheric during xenolith's transport to the surface results in *in situ* partial melting inside gabbro nodules followed then by re-equilibration of the interstitial melts with the surrounding solid phases and formation of the thin, micron-sized rims on the composing OL, CPX and PL. Furthermore, such pressure release could also cause partial to complete disintegration of the present gabbro fragments. The eruption of magmas in the sub-glacial environment finishes the process, resulting in very clear, microphenocryst-free pillow-rim glasses and negligible degree of interstitial melt crystallization inside gabbro nodules; low, obviously degassed concentrations of S in the host pillow-rims, glassy crusts and interstitial glasses support this conclusion.

Implications for Sr enrichment in MORB and OIB

Iceland is not the single location where such Sr enrichment in primitive basaltic melts has been described. There are several regions on the mid-ocean ridge, for example, Siqueiros Fracture Zone in Pacific (Sobolev et al. 1992; Danyushevsky et al. 2003, 2004), 43°N on the Mid-Atlantic Ridge (Kamenetsky et al. 1998), where similar, relatively high Sr contents in primitive MORB magmas were reported. Two concurrent models of melt–rock reaction/melting in the mantle (43°N MAR; Kamenetsky et al. 1998) versus assimilation of gabbroic material from crystal mush zone (Siqueiros FZ; Danyushevsky et al. 2003, 2004) were proposed. In particular, Danyushevsky et al. (2003, 2004) have analyzed in detail various mechanisms of origin so-called “anomalous melt inclusions” characterizing, in particular, by such pronounced Sr excess and proposed a dissolution-reaction-mixing (DRM) model acting at the grain-size scale. The main results obtained by these authors are very close to our present results. However, there is one critical point in application of the DRM model *i.e.*, melting of PL-rich rocks alone is unable to produce depletion of Ba relative to Nb in partial melts in the presence of PL as a residual phase. Most of the glass inclusions and pillow-rim glasses from 43°N MAR exhibit systematic enrichment of Ba relative to Nb and thus, are more likely to be consistent with the DRM model. The Siqueiros glasses, in contrast, are not (*e.g.*, Fig. 5 in Danyushevsky et al. 2003). We suggest, therefore, that the model of melt percolation which satisfactorily explains the geochemical signature of the Icelandic glasses could also be employed for Siqueiros FZ in order to explain the origin of Sr-enriched magmas described by Sobolev et al. (1992) and Danyushevsky et al. (2003, 2004). In summary, we propose that the process of melt percolation is not exclusively restricted to Iceland, the region characterized by anomalously thick oceanic

crust, but represents a process that may often occur within normal mid-ocean ridge segments as well.

Strontium-enriched melt inclusions were also reported in olivines from Mauna Loa shield tholeiites, Hawaii by Sobolev et al. (2000). In contrast to our results, the Sobolev et al. (2000) data were interpreted as a feature of a mantle source, rather than the result of interaction of magmas with PL-bearing crustal rocks. The reasoning for this interpretation was based on the fact that the Mauna Loa lavas and associated with them Sr-rich melt inclusions in olivine are severely undersaturated with plagioclase and thus, could not be involved in the reaction with PL-bearing crustal lithologies. Thus, Sobolev et al. (2000, 2005) have suggested that the geochemical features of PL-bearing crustal rocks (namely gabbros) were incorporated in the Hawaiian mantle source via their consequent recycling, melting and reacting with peridotite at high pressures. We emphasize that this feature called “ghost plagioclase” is in contrast to that of the Midfell volcanism, SW Iceland, as well as probably to several manifestations of the volcanism of mid-oceanic ridges (Siqueiros Fracture Zone in Pacific or 43°N on the Mid-Atlantic Ridge; Sobolev et al. 1992; Kamenetsky et al. 1998; Danyushevsky et al. 2003, 2004). All these magmas, in contrast to Mauna Loa (Sobolev et al. 2000, 2005), are saturated or are close to saturation with plagioclase and clinopyroxene at low, crustal pressures. The saturation of melt with plagioclase *i.e.*, “live plagioclase signature” is an essential requirement for the proposed model describing melt–gabbro interaction in the Midfell magmas.

Summary and conclusions

1. Gabbro xenoliths from the Midfell basaltic to picritic pillow lavas represent fragments of a solidified crystal mush playing the role of chromatographic columns for primitive, tholeiitic magmas percolating through and related to the neovolcanic rift zone of Iceland.
2. These primitive magmas were not originally enriched in CaO and depleted in Al₂O₃, and did not possess a pronounced Sr excess in the chondrite-normalized trace element spectra. Such Ca and Sr enrichments and Al depletion are exclusively related to the melt percolation through gabbroic rocks occurred within the thick Icelandic crust at relatively low pressures.
3. The Midfell gabbroic rocks experienced at least three main stages in their history before being trapped by erupting magma and transported to the surface as xenoliths. Stage 1 is earlier crystallization of PL + CPX ± OL ± SP gabbro cumulates from the melts which are compositionally similar to the transporting magmas; their crystallization occurred in the magma reservoirs located at about 10 km depth (ca. 350 MPa lithostatic pressure) corresponding to the depth of Layer 3 in the crust

section beneath the neovolcanic rift zone of Iceland. Stage 2 includes percolation of geochemically similar tholeiitic magmas through earlier formed OL–CPX–PL crystal mush or solidified gabbroic layer in the temperature range between 1,190–1,230°C and at similar pressures of 350 MPa. This stage may also include selective crystallization and dissolution of clinopyroxene crystals deposited in the cumulative layer, causing formation of large clinopyroxene oikocrysts. Stage 3 comprises fragmentation of a brittle, cumulative gabbro layer followed by nearly adiabatic transport of the rock fragments to the surface.

4. We emphasize that melt percolation through gabbroic rocks is responsible for the pronounced Sr excess observed in many Icelandic tholeiitic rocks and may represent a process to be also widespread within normal mid-ocean ridge segments. The Sr-enrichment of PL-undersaturated magmas (i.e., so-called “ghost plagioclase signature”) could not be, however, produced by this type of process.

Acknowledgments We thank Alan Boudreau for fruitful discussions and rapid correction of several program bugs which appeared during our exploration and testing of the IRIDIUM 5.10 Beta version, Astri Kvassnes for thorough informal review and helpful comments to the earlier manuscript version, Museum of Natural History, Washington DC, who kindly provided us with standards for electron microprobe analysis. Formal reviews by Alan Boudreau, Christian Tegner and Vadim Kamenetsky helped us to substantially improve the manuscript. Editorial handling by J. Hoefs is acknowledged. This work was supported by Wolfgang Paul Award, Alexander von Humboldt Foundation, to AVS, and the Max-Planck Society. Partial support of DFG (Project HO 1026/16-1), RFBR (06-05-65234-a) and President of Russian Federation Foundation (HIII-4264.2006.5) to AVS is also acknowledged.

References

- Anders E, Grevesse N (1989) Abundances of the elements: meteoritic and solar. *Geochim Cosmochim Acta* 53:197–214
- Ariskin AA, Barmina GS (1990) Equilibria thermometry between plagioclases and basalt or andesite magmas. *Geochem Int* 27(10):129–134
- Ariskin AA, Barmina GS, Frenkel MYa (1987) Simulating low-pressure tholeiite-magma crystallization at a fixed oxygen fugacity. *Geochem Int* 24(5):92–100
- Ariskin AA, Frenkel MY, Barmina GS, Nielsen R (1993) CO-MAGMAT: a FORTRAN program to model magma differentiation processes. *Comput Geosci* 19:1155–1170
- Batanova VG, Suhr G, Sobolev AV (1998) Origin of geochemical heterogeneity in the mantle peridotites from the Bay of Islands ophiolite, Newfoundland, Canada: ion probe study of clinopyroxenes. *Geochim Cosmochim Acta* 62:853–866
- Beblo M, Björnsson A (1978) Magnetotelluric investigation of the lower crust and upper mantle beneath Iceland. *J Geophys* 45:1–16
- Beblo M, Björnsson A (1980) A model of electrical resistivity beneath NE Iceland, correlation with temperature. *J Geophys* 47:184–190
- Beblo M, Björnsson A, Arnason K, Stein B, Woldgram P (1983) Electrical conductivity beneath Iceland: constraints imposed by magnetotelluric results on temperature, partial melt, crust and mantle structure. *J Geophys* 53:16–23
- Björnsson A (1977) Electrical resistivity of layer 3 in the Icelandic crust. *Soc Sci Isl, Greinar* V:7–23
- Björnsson A (1985) Dynamics of crustal rifting in NE Iceland. *J Geophys Res* 90:10151–10162
- Bodinier JL, Vasseur G, Vernieres J, Dupuy C, Fabries J (1990) Mechanisms of mantle metasomatism: geochemical evidence from the Lherz orogenic peridotite. *J Petrol* 31:597–628
- Boudreau AE (2003) IRIDIUM—a program to model reaction of silicate liquid infiltrating a porous solid assemblage. *Comp Geosci* 29:423–429
- Boudreau AE, Meurer WP (1999) Chromatographic separation of the platinum-group elements, gold, base metals and sulfur during degassing of a compacting and solidifying crystal pile. *Contrib Mineral Petrol* 134:174–185
- Carignan J, Hild P, Mevelle G, Morel J, Yeghicheyan DE (2001) Routine analyses of trace element in geological samples using flow injection and low pressure on-line liquid chromatography coupled to ICP-MS: a study of geochemical reference materials BR, DR-N, UB-N, AN-G and GH. *Geostand Newsl* 25:187–198
- Chauvel C, Hémond C (2000) Melting of a complete section of recycled oceanic crust: trace element and Pb isotopic evidence from Iceland. *Geochem Geophys Geosyst* 1:1999GC000002
- Christensen NI (1974) The petrologic nature of the lower oceanic crust and upper mantle. In: *Geodynamics of Iceland and the North Atlantic Area*. Reidel, Dordrecht, pp 165–176
- Danyushevsky LV (2001) The effect of small amounts of H₂O on crystallization of mid-ocean ridge and backarc basin magmas. *J Volcanol Geotherm Res* 110:265–280
- Danyushevsky LV, Sobolev AV, Dmitriev LV (1996) Estimation of the pressure of crystallization and H₂O content of MORB and BABB glasses: calibration of an empirical technique. *Mineral Petrol* 57:185–204
- Danyushevsky LV, Perfit MR, Eggins SM, Falloon TJ (2003) Crustal origin for coupled “ultra-depleted” and “plagioclase” signatures in MORB olivine-hosted melt inclusions: evidence from the Siqueiros Transform Fault, East Pacific Rise. *Contrib Mineral Petrol* 144:619–637
- Danyushevsky LV, Leslie RAJ, Crawford AJ, Durance P (2004) Melt inclusions in primitive olivine phenocrysts: the role of localized reaction processes in the origin of anomalous compositions. *J Petrol* 45: 2531–2553
- Darbyshire FA, White RS, Priestley KF (2000) Structure of the crust and uppermost mantle of Iceland from a combined seismic and gravity study. *Earth Planet Sci Lett* 181:409–428
- Dixon JE, Clague DA, Stolper EM (1991) Degassing history of water, sulfur and carbon in submarine lavas from Kilauea volcano, Hawaii. *J Geol* 99:371–394
- Fahey AJ, Zinner EK, Crozaz G, Kornacki AS (1987) Microdistributions of Mg isotopes and REE abundances in a Type A calcium–aluminum-rich inclusion from Efremovka. *Geochim Cosmochim Acta* 51:3215–3229
- Falloon T, Green DH, Danyushevsky LV, Faul UH (1999) Peridotite melting at 1.0 and 1.5 GPa: an experimental evaluation of techniques using diamond aggregates and mineral mixes for determination of near-solidus melts. *J Petrol* 40:1343–1375
- Flóvenz OG, Gunnarsson K (1991) Seismic crustal structure in Iceland and surrounding area. *Tectonophys* 189:1–17
- Ford CE, Russel DG, Craven JA, Fisk MR (1983) Olivine–liquid equilibria: temperature, pressure and composition dependence of the crystal/liquid cation partition coefficients for Mg, Fe²⁺, Ca and Mn. *J Petrol* 24:256–265
- Genshaft YuS, Saltykovsky AJA (1999) Iceland: deep structure, evolution, and intrusive magmatism. GEOS, Moscow
- Ghiorso MS, Sack RO (1995) Chemical mass transfer in magmatic processes IV A revised and internally consistent thermodynamic model for the interpolation and extrapolation of liquid–solid equilibria in magmatic systems at elevated temperatures and pressures. *Contrib Mineral Petrol* 119:197–212
- Gurenko AA, Chaussidon M (1995) Enriched and depleted primitive melts included in olivine from Icelandic tholeiites: origin

- by continuous melting of a single mantle column. *Geochim Cosmochim Acta* 59:2905–2917
- Gurenko AA, Chaussidon M (2002) Oxygen isotope variations in primitive tholeiites of Iceland: evidence from a SIMS study of glass inclusions, olivine phenocrysts and pillow rim glasses. *Earth Planet Sci Lett* 205: 63–79
- Gurenko AA, Sobolev AV, Polyakov AI, Kononkova NN (1988) Primary melt of the Iceland rift tholeiites: the composition and conditions of crystallization (in Russian). *Doklady Akademii Nauk SSSR* 301:179–184
- Gurenko AA, Sobolev AV, Kononkova NN (1990) Petrology of primary melt of riftogenic tholeiites from Reikjanes Peninsula, Iceland (in Russian). *Geokhimiya* 8:1137–1150
- Gurenko AA, Chaussidon M, Sobolev AV (2004) Oxygen isotopes in zoned Icelandic olivines: implications for magma residence time. In: Altherr R (ed) *Kurzfassungen der Vorträge und Poster 82. Jahrestagung der Deutschen Mineralogischen Gesellschaft, Karlsruhe, Germany, E. Schweizerbart'sche Verlagsbuchhandlung (Nägele u. Obermiller), Stuttgart*, p 50
- Halliday AN, Lee D-C, Tommasini S, Davies GR, Paslick CR, Fitton JG, James DE (1995) Incompatible trace elements in OIB and MORB and source enrichment in the sub-oceanic mantle. *Earth Planet Sci Lett* 133: 379–395
- Hansteen TH (1991) Multi-stage evolution of the picritic Maelifell rocks, SW Iceland: constraints from mineralogy and inclusions of glass and fluid in olivine. *Contrib Mineral Petrol* 109:225–239
- Hart SR, Blusztajn J, Dick HJB, Meyer PS, Muehlenbachs K (1999) The fingerprint of seawater circulation in a 500-meter section of ocean crust gabbros. *Geochim Cosmochim Acta* 63:4059–4080
- Hémond C, Arndt NT, Lichtenstein U, Hofmann AW, Oskarsson N, Steinthorsson S (1993) The heterogeneous Iceland plume: Nd–Sr–O isotopes and trace element constraints. *J Geophys Res* 98:15833–15850
- Hernance JF, Grillo LR (1974) Constraints on temperatures beneath Iceland from magnetotelluric data. *Phys Earth Planet Int* 8:1–12
- Høj JW (1993) Gabbro–anorthosite nodules from the Krisuvik fissure system and active zone of rifting, Reykjanes peninsula, SW Iceland. *N Jahrb Miner Abh* 165:169–189
- Jakobsson S (1966) The Grimsmes lavas, SW-Iceland. *Acta Naturalia Islandica* 2:5–30
- Jakobsson SP (1979) Outline of the petrology of Iceland. *Jökull* 29: 57–73
- Jakobsson SP, Pedersen AK, Rönsbo JG, Larsen LM (1973) Petrology of mugearite–hawaiite: early extrusives in the 1973 Heimaey eruption, Iceland. *Lithos* 6:203–214
- Jakobsson SP, Jónsson J, Shido F (1978) Petrology of the Western Reykjanes Peninsula, Iceland. *J Petrol* 19:669–705
- Jarosewich EJ, Nelen JA, Norberg JA (1980) Reference samples for electron microprobe analyses. *Geostand Newslett J Geostand Geoanalys* 4:43–47
- Jochum KP, Dingwell DB, Rocholl A, Stoll B, Hofmann AW, Becker S, Bismehn A, Bessette D, Dietze H-J, Dulski P, Erzinger J, Hellebrand E, Hoppe P, Horn I, Janssens K, Jenner GA, Klein M, McDonough WF, Maetz M, Mezger K, Münker C, Nikogosian IK, Pickhardt C, Raczek I, Rhede D, Seufert HM, Simakin SG, Sobolev AV, Spettel B, Straub S, Vincze L, Wallianos A, Weckwerth G, Weyer S, Wolf D, Zimmer M (2000) The preparation and preliminary characterization of eight geological MPI-DING reference glasses for in-situ microanalysis. *Geostand Newslett J Geostand Geoanalys* 24:87–133
- Kamenetsky VS, Eggins SM, Crawford AJ, Green DH, Gasparon M, Falloon TJ (1998) Calcic melt inclusions in primitive olivine at 43°N MAR: evidence for melt–rock reaction/melting involving clinopyroxene-rich lithologies during MORB generation. *Earth Planet Sci Lett* 160:115–132
- Kinzler RJ, Grove TL (1992a) Primary magmas of mid-ocean ridge basalts 1. Experiments and methods. *J Geophys Res* 97:6885–6906
- Kinzler RJ, Grove TL (1992b) Primary magmas of mid-ocean ridge basalts 2. Applications. *J Geophys Res* 97:6907–6926
- Kristmannsdóttir H (1971) Anorthosite inclusions in Tertiary dolerite from the island groups Hrapsey and Purkey, West Iceland. *J Geol* 79: 741–748
- Larsen JG (1979) Glass-bearing gabbro inclusions in hyaloclastites from Tindfjalljökull, Iceland. *Lithos* 12:289–302
- Marsh BD (1995) Solidification fronts and magmatic evolution. *Mineral Mag* 60:5–40
- Marsh BD (1998) On the interpretation of crystal size distribution in magmatic systems. *J Petrol* 39:553–599
- McKenzie D (1984) The generation and compaction of partially molten rock. *J Petrol* 25:713–765
- Navon O, Stolper E (1987) Geochemical consequences of melt percolation: the upper mantle as a chromatographic column. *J Geol* 95:285–307
- Nimis P (1995) A clinopyroxene geobarometer for basaltic systems based on crystal-structure modelling. *Contrib Mineral Petrol* 121:115–125
- Oskarsson N, Sigvaldason GE, Steinthorsson S (1982) A dynamic model of rift zone petrogenesis and regional petrology of Iceland. *J Petrol* 23: 28–74
- Oskarsson N, Steinthorsson S, Sigvaldason GE (1985) Iceland geochemical anomaly: origin, volcanotectonics, chemical fractionation and isotope evolution of the crust. *J Geophys Res* 90:10011–10026
- Pálmason G (1971) Crustal structure of Iceland from explosion seismology. *Visindafélag Isl Rit* 40:9–187
- Pálmason G (1973) Kinematics and heat flow in a volcanic rift zone, with application to Iceland. *Geophys JR Astron Soc* 33:451–481
- Pálmason G (1980) A continuum model of crustal generation in Iceland; kinematic aspects. *J Geophys* 47:7–18
- Pedersen AK, Hald N (1982) A cummingtonite–porphyritic dacite with amphibole-rich xenoliths from the Tertiary central volcano at Króksfjörður, NW Iceland. *Lithos* 15:137–159
- Risku-Norja H (1985) Gabbro nodules from picritic pillow basalt, SW Iceland. *Nordic Volcanological Institute Prof Paper* 8501:32–49
- Shaw DM (1970) Trace element fractionation during anatexis. *Geochim Cosmochim Acta* 34:237–243
- Sigurðsson IA (1989) *Gabbróhnyðlingar í Hraunsvík á Reykjaneskaga*. Reykjavík, Háskóli Íslands Raunvísindadeild, pp 67
- Skovgaard AC, Storey M, Baker J, Blusztajn J, Hart SR (2001) Osmium–oxygen isotopic evidence for a recycled and strongly depleted component in the Iceland mantle plume. *Earth Planet Sci Lett* 194: 259–275
- Sobolev AV, Casey JF, Shimizu N, Perfit MR (1992) Contamination and mixing of MORB primary melts: evidence from melt inclusions in Siqueiros picrites. *Eos Trans AGU*, 73 (14), Spring Meet Suppl:336
- Sobolev AV, Gurenko AA, Shimizu N (1994) Ultra-depleted melts from Iceland: data from melt inclusion studies. *Mineral Mag* 58A:860–861
- Sobolev AV, Hofmann AW, Nikogosian IK (2000) Recycled oceanic crust observed in “ghost plagioclase” within the source of Mauna Loa lavas. *Nature* 404:986–990
- Sobolev AV, Hofmann AW, Sobolev SV, Nikogosian IK (2005) An olivine-free mantle source of Hawaiian shield basalts. *Nature* 434:590–597
- Steinthorsson S, Oskarsson N, Sigvaldason GE (1985) Origin of alkali basalts in Iceland: a plate tectonic model. *J Geophys Res* 90: 10027–10042
- Thayer RE, Björnsson LA, Alvarez L, Hernance JR (1981) Magma genesis and crustal spreading in the northern neovolcanic zone in Iceland: telluric–magnetotelluric constraints. *Geophys JR Astron Soc* 65: 423–442
- Thorarinsson S (1953) *Graenavatn and Gestsstadavatn*. *Geografisk Tidsskrift* 52:292–302
- Thordarson T, Self S, Oskarsson N, Hulsebosch T (1996) Sulfur, chlorine, and fluorine degassing and atmospheric loading by the

- 1783–1784 AD Laki (Skaftár Fires) eruption in Iceland. *Bull Volcanol* 58:205–225
- Trønnes RG (1990) Basaltic melt evolution of the Hengill Volcanic System, SW Iceland, and evidence for clinopyroxene assimilation in primitive tholeiitic magmas. *J Geophys Res* 95:15893–15910
- Tryggvason T (1960) The gabbro bombs at lake Graenavatn. *Bull Geol Inst Univ Uppsala* 38:1–5
- Weaver JS, Langmuir CH (1990) Calculation of phase equilibrium in mineral–melt systems. *Comput Geosci* 16:1–19
- White WM (1997) *Geochemistry*. An on-line text-book. Cornell University, URL: <http://www.geo.cornell.edu/geology/classes/geo455/Chapters.html>
- Zinner E, Crozaz G (1986) A method for the quantitative measurement of rare earth elements in the ion microprobe. *Int J Mass Spectr Ion Proc* 69:17–38